The Astrophysical Journal Letters, 990:L10 (17pp), 2025 September 1 https://doi.org/10.3847/2041-8213/adf113

exoALMA. XVIII. Interpreting Large-scale Kinematic Structures as Moderate Warping

Andrew J. Winter[1], Myriam Benisty[2], Andrés F. Izquierdo[3,4,5,6], Giuseppe Lodato[7], Richard Teague[8], Carolin N. Kimmig[7], Sean M. Andrews[9], Jaehan Bae[3], Marcelo Barraza-Alfaro[8], Nicolás Cuello[10], Pietro Curone[11], Ian Czekala[12], Stefano Facchini[7], Daniele Fasano[13], Cassandra Hall[14,15,16], Caitlyn Hardiman[17], Thomas Hilder[17], John D. Ilee[18], Misato Fukagawa[19], Cristiano Longarini[7,20], François Ménard[10], Ryuta Orihara[21], Christophe Pinte[10], Daniel J. Price[17], Giovanni Rosotti[7], Jochen Stadler[13], David J. Wilner[9], Lisa Wölfer[8], Hsi-Wei Yen[22], Tomohiro C. Yoshida[19,23], and Brianna Zawadzki[24]

[1] Astronomy Unit, School of Physics and Astronomy, Queen Mary University of London, London E1 4NS, UK; andrew.winter@qmul.ac.uk
[2] Max-Planck Institute for Astronomy (MPIA), Königstuhl 17, 69117 Heidelberg, Germany
[3] Department of Astronomy, University of Florida, Gainesville, FL 32611, USA
[4] Leiden Observatory, Leiden University, P.O. Box 9513, NL-2300 RA Leiden, The Netherlands
[5] European Southern Observatory, Karl-Schwarzschild-Str. 2, D-85748 Garching bei München, Germany
[6] NASA Hubble Fellowship Program Sagan Fellow, USA
[7] Dipartimento di Fisica, Università degli Studi di Milano, Via Celoria 16, 20133 Milano, Italy
[8] Department of Earth, Atmospheric, and Planetary Sciences, Massachusetts Institute of Technology, Cambridge, MA 02139, USA
[9] Center for Astrophysics | Harvard & Smithsonian, Cambridge, MA 02138, USA
[10] Univ. Grenoble Alpes, CNRS, IPAG, 38000 Grenoble, France
[11] Departamento de Astronomía, Universidad de Chile, Camino El Observatorio 1515, Las Condes, Santiago, Chile
[12] School of Physics & Astronomy, University of St. Andrews, North Haugh, St. Andrews KY16 9SS, UK
[13] Université Côte d'Azur, Observatoire de la Côte d'Azur, CNRS, Laboratoire Lagrange, France
[14] Department of Physics and Astronomy, The University of Georgia, Athens, GA 30602, USA
[15] Center for Simulational Physics, The University of Georgia, Athens, GA 30602, USA
[16] Institute for Artificial Intelligence, The University of Georgia, Athens, GA 30602, USA
[17] School of Physics and Astronomy, Monash University, Clayton VIC 3800, Australia
[18] School of Physics and Astronomy, University of Leeds, Leeds, UK, LS2 9JT, UK
[19] National Astronomical Observatory of Japan, Osawa 2-21-1, Mitaka, Tokyo 181-8588, Japan
[20] Institute of Astronomy, University of Cambridge, Madingley Road, CB3 0HA, Cambridge, UK
[21] Department of Astronomy, Graduate School of Science, The University of Tokyo, 7-3-1 Hongo, Bunkyo-ku, Tokyo 113-0033, Japan
[22] Academia Sinica Institute of Astronomy & Astrophysics, 11F of Astronomy-Mathematics Building, AS/NTU, No. 1, Sec. 4, Roosevelt Road, Taipei 10617, Taiwan
[23] Department of Astronomical Science, The Graduate University for Advanced Studies, SOKENDAI, 2-21-1 Osawa, Mitaka, Tokyo 181-8588, Japan
[24] Department of Astronomy, Van Vleck Observatory, Wesleyan University, 96 Foss Hill Drive, Middletown, CT 06459, USA

Received 2025 June 26; revised 2025 July 14; accepted 2025 July 15; published 2025 August 27

Abstract

The exoALMA program gave an unprecedented view of the complex kinematics of protoplanetary disks, revealing diverse structures that remain poorly understood. We show that moderate disk warps ($\sim 0\overset{\circ}{.}5$–$2^\circ$) can naturally explain many of the observed large-scale velocity features with azimuthal wavenumber $m = 1$. Using a simple model, we interpret line-of-sight velocity variations as changes in the projected Keplerian rotation caused by warping of the disk. While not a unique explanation, this interpretation aligns with growing observational evidence that warps are common. We demonstrate that such warps can also produce spiral structures in scattered light and CO brightness temperature, with $\sim$10 K variations in MWC 758. Within the exoALMA sample, warp properties correlate with stellar accretion rates, suggesting a link between the inner disk and outer disk kinematics. If warps cause large-scale kinematic structure, this has far-reaching implications for turbulence, angular momentum transport, and planet formation.

Unified Astronomy Thesaurus concepts: Protoplanetary disks (1300); Hydrodynamics (1963); Astronomy data analysis (1858); Pre-main sequence stars (1290)

Materials only available in the online version of record: figure set

1. Introduction

The Atacama Large Millimeter/submillimeter Array (ALMA) Large Program exoALMA has provided an unprecedented view of the outer kinematic structure of protoplanetary disks (R. Teague et al. 2025). Through high-resolution observations of the ^{12}CO and ^{13}CO $J = 3$–2 emission lines in particular (R. A. Loomis et al. 2025; B. Zawadzki et al. 2025), the survey has revealed that disk kinematics are often asymmetric, exhibiting large-scale deviations from simple Keplerian rotation (A. F. Izquierdo et al. 2025; J. Stadler et al. 2025, M. Fukagawa et al. 2025, in preparation). While many of these features can plausibly be linked to local perturbations, such as planets (C. H. Gardner et al. 2025; C. Pinte et al. 2025), instabilities (M. Barraza-Alfaro et al. 2025), or laminar flows (A. Zuleta et al. 2024), explaining the largest-scale structure remains an important open challenge.

A recurring pattern in these data is the presence of $m = 1$–like azimuthal asymmetries in the line-of-sight (LOS) velocity fields. These features often extend across large portions of the disk and appear in most exoALMA targets to varying degrees, suggesting a global, disk-scale origin. Intriguingly, simulations have shown that disk warping can produce similar kinematic behavior (A. K. Young et al. 2022). In this Letter, we explore the hypothesis that such features can arise from moderate warping of the disk plane. Specifically, we consider smooth radial variations in inclination and position angle of a few degrees. In doing so, we demonstrate that such warps may account not only for the widespread, coherent, low-amplitude kinematic asymmetries observed in the outer disk but also for corresponding features in scattered light and brightness temperature.

The theory of disk warping has a long and well-developed history, with foundational predictions dating back to early studies of viscous accretion flows with misaligned angular momentum (J. C. B. Papaloizou & J. E. Pringle 1983; J. E. Pringle 1996). In the low-viscosity regime typical of protoplanetary disks ($H/R \gtrsim \alpha$, where α is the canonical turbulence parameter, H is the disk pressure scale height, and R is the cylindrical radius in disk coordinates), warps are expected to propagate as bending waves. These travel at the local sound speed and are damped over a timescale $\tau_{\rm damp} \sim 1/\alpha\Omega_{\rm K}$, where $\Omega_{\rm K}$ is the Keplerian frequency (S. H. Lubow & G. I. Ogilvie 2000; G. I. Ogilvie & H. N. Latter 2013). This means that $\tau_{\rm damp} \sim 1$ Myr for $\alpha \sim 10^{-4}$ at 100 au around a solar-mass star. Internal torques between neighboring disk rings—driven by pressure gradients and resonant radial, azimuthal, and vertical motions ("sloshing" and "breathing" modes; e.g., G. Lodato & J. E. Pringle 2007; C. P. Dullemond et al. 2022; L. E. Held & G. I. Ogilvie 2024)—further shape the global disk structure. In addition, parametric instability can be excited via resonance between vertical shear and inertial waves (G. I. Ogilvie & H. N. Latter 2013; S.-J. Paardekooper & G. I. Ogilvie 2019), potentially generating strong turbulence and accelerating warp decay (H. Deng & G. I. Ogilvie 2022). Counterintuitively, warping may not only produce dust substructures (C. Longarini et al. 2021) but also promote rapid dust settling into the midplane (H. Aly et al. 2024).

In cases of extreme warping, large misalignments can lead to disk breaking, in which the disk separates into discrete planes (e.g., G. Lodato & D. J. Price 2010; S. Facchini et al. 2013, 2018; C. Nixon et al. 2013; S. Doğan et al. 2023; A. K. Young et al. 2023), resulting in precessing shadows (R. Nealon et al. 2020). These shadows may in turn have a dramatic impact on disk structure (S. Zhang & Z. Zhu 2024; A. Ziampras et al. 2025). The narrow shadows (e.g., in the sample of A. J. Bohn et al. 2022) require large inner disk misalignments that imply a torn disk ($\gg H/R$; e.g., D. J. Price et al. 2018; R. Nealon et al. 2020). Meanwhile, both geometric (G. A. Muro-Arena et al. 2020; J. Debes et al. 2023) and dynamical (R. Nealon et al. 2018, 2019) models show that modest warps give rise to broad shadows in scattered light, which extend over ~180° in azimuth. This work pertains to these more moderate warp structures, although misaligned (torn) inner disks are plausibly related phenomena.

Observational evidence for widespread warping and misaligned inner disks is growing. High-contrast imaging in the near-infrared (NIR) has revealed shadows in numerous systems (M. Benisty et al. 2023), for example, TW Hydra (J. H. Debes et al. 2016; J. Debes et al. 2023), HD 142527, and DoAr 44 (e.g., S. Casassus et al. 2018). "Dipper" optical or NIR light curves are common and often interpreted as occultation by warped or misaligned inner disks (A. M. Cody et al. 2014; J. Stauffer et al. 2015; M. Ansdell et al. 2016b, 2016a). At millimeter wavelength, molecular line observations have indicated kinematic misalignments in systems such as HD 100546 and HD 142527 (J. E. Pineda et al. 2014; S. Casassus et al. 2015), although misalignments can be difficult to distinguish from radial flows (K. A. Rosenfeld et al. 2014; A. Zuleta et al. 2024). VLTI/GRAVITY observations of disks with shadows show that several of the cases have unambiguous misalignments between inner and outer disks (A. J. Bohn et al. 2022). Hubble Space Telescope (e.g., A. M. Watson & K. R. Stapelfeldt 2007) and more recently JWST scattered light observations have shown asymmetric lobes above and below the midplane of edge-on disks, as well as appearing among ~75% in the sample of M. Villenave et al. (2023). These lobes vary in relative brightness with wavelength, suggestive of an inner disk misalignment or moderate warp (A. Juhász & S. Facchini 2017; R. Nealon et al. 2019; C. N. Kimmig & M. Villenave 2025).

The origin of disk warping remains an open question. While a rotation axis of the star tilted with respect to the magnetic field or inner disk may cause inner disk misalignment (e.g., D. Lai 1999; F. Foucart & D. Lai 2011; M. M. Romanova et al. 2021), it is not clear whether this applies to the moderate warping at larger spatial scales we explore in this work. Large-scale warps in the outer disk may still be caused by magnetic fields, or they may be self-induced owing to radiation-driven instability (J. E. Pringle 1996; P. J. Armitage & J. E. Pringle 1997), driven by perturbations from companions or flybys (S. Kraus et al. 2020; R. Nealon et al. 2020; N. Cuello et al. 2023) or late infall of material (M. Kuffmeier et al. 2023). Misaligned stellar or substellar companions can torque the disk and induce warps or even disk breaking (e.g., R. Nealon et al. 2018; Z. Zhu 2019). However, for systems not in stellar multiples, flybys are not expected to be common (G. P. Rosotti et al. 2014; L. Shuai et al. 2022; A. J. Winter et al. 2024b). Alternatively, continued infall of misaligned material from the surrounding envelope can reorient the outer disk while the inner disk remains aligned with the stellar spin (e.g., M. R. Bate et al. 2010; M. Kuffmeier et al. 2024), with an increasing number of observational case studies (C. Ginski et al. 2021; A. Garufi et al. 2024). These mechanisms may help to explain the growing body of observational evidence pointing to misalignment between inner and outer disk structures.

In this work, we systematically apply a simple warp model to the exoALMA sample, using residual velocity maps derived from Keplerian fitting. Our goal is to determine whether coherent warps can explain the $m = 1$ structure seen in many disks and to explore possible physical correlations with other system properties such as accretion rate and nonaxisymmetry in the dust. We show that moderate warps can account for the large-scale structure in many systems, with implications for our understanding of angular momentum transport and the physical state of protoplanetary disks.

2. Methodology

2.1. Data

We aim to explore whether radially dependent perturbations to inclination and position angle (i.e., a warped disk) can explain the nonaxisymmetric structures in the LOS velocity in the exoALMA data set (for an overview, see R. Teague et al. 2025). We restrict ourselves to the fiducial resolution ^{12}CO LOS residual velocity maps ($\delta v_{\rm los}$) obtained through the DISCMINER fitting procedure (A. F. Izquierdo et al. 2025).

Unless otherwise stated, we always use the outcome of the analysis pipeline performed on continuum-subtracted cubes, with a nominal beam size of 0.″15 and channel spacing 100 m s^{-1}, clipped at 3σ. We apply our procedure on residuals obtained from the DISCMINER analysis, which models the channel maps in terms of a fixed inclination and position angle, with a parameterized emission surface height and intensity, and a Keplerian rotation curve. The residuals are deprojected and defined with the azimuthal coordinate $\phi = 0$ along the redshifted major axis.

2.2. Linear Approximation

While we note that tools exist in the literature to model the kinematics of warped disks (S. Casassus & S. Pérez 2019; S. Casassus 2022), we aim to achieve a very simple, flexible model that is easy to apply without fitting numerous parameters. Our method is similar to the "tilted ring" approach that has been applied historically to modeling galaxy rotation curves (e.g., K. G. Begeman 1989). We aim not to fully fit radial, vertical, and azimuthal velocity variations but to interpret all LOS variations as far as possible as being due to the projection of the Keplerian azimuthal component. This allows us to efficiently fit for radially dependent profiles in the warp structure, but our results should be interpreted as a "maximal" tilt amplitude that could be inferred from the data.

In order to model the observed perturbations as warped disks, we start by assuming a circular ring of material orbiting with azimuthal velocity:

$$\boldsymbol{v} = v_\phi(R)\,\hat{e}_\phi, \qquad \text{with } v_\phi(R) = \pm\sqrt{\frac{GM_*}{R}}, \tag{1}$$

where we will assume hereafter that v_ϕ is positive. The unperturbed LOS velocity (with fixed inclination i_0 and position angle PA$_0$) is then

$$v_{\rm los}^{\rm flat}(R, \phi) = v_\phi(R)\sin i_0 \cos(\phi - {\rm PA}_0). \tag{2}$$

Without loss of generality, we will take PA$_0 = 0$ to simplify the following expressions, and we rotate all disks to conform to this definition in figures ($\phi = 0$ corresponding to the redshifted semimajor axis).

Now, if we allow the disk orientation (inclination and position angle) to vary with radius,

$$i = i_0 + \delta i(R), \tag{3}$$

$${\rm PA} = {\rm PA}_0 + \delta{\rm PA}(R). \tag{4}$$

If we assume small perturbations (δi, $\delta{\rm PA} \ll 1$ in radians), then

$$\sin(i_0 + \delta i) \approx \sin i_0 + \delta i \cos i_0, \tag{5}$$

$$\cos(\phi - \delta{\rm PA}) \approx \cos\phi + \delta{\rm PA}\sin\phi. \tag{6}$$

Substituting into the projected velocity,

$$v_{\rm los}^{\rm warp} \approx v_\phi(R)[(\sin i_0 + \delta i \cos i_0)(\cos\phi + \delta{\rm PA}\sin\phi)] \tag{7}$$

$$\approx v_\phi(R)[\sin i_0\cos\phi + \delta i\cos i_0\cos\phi + \delta{\rm PA}\sin i_0\sin\phi]. \tag{8}$$

Thus, the residual in the LOS velocity is

$$\delta v_{\rm los} = v_{\rm los}^{\rm warp} - v_{\rm los}^{\rm flat} = v_\phi(R)[\delta i(R)\cos i_0\cos\phi + \delta{\rm PA}(R)\sin i_0\sin\phi]. \tag{9}$$

We can rewrite Equation (9) as

$$\delta v_{\rm los}(R, \phi) = A(R)\cos\phi + B(R)\sin\phi. \tag{10}$$

We can then derive the inclination and position angle perturbations from the coefficients $A(R)$ and $B(R)$ as

$$\delta i(R) = \frac{A(R)}{v_\phi(R)\cos i_0}, \tag{11}$$

$$\delta{\rm PA}(R) = \frac{B(R)}{v_\phi(R)\sin i_0}. \tag{12}$$

The coefficients $A(R)$ and $B(R)$ are obtained by least-squares fitting[25] to the azimuthal slice of the residual field in each annulus.[26] We then assume an uncertainty equivalent to the square root of the residual rms sum divided by the number of beams that fit within $2\pi R$. This should be interpreted as a statistical uncertainty, not one that necessarily accounts for all the possible systematics inherent in the complexity of the exoALMA pipeline. In addition, as we discuss in Section 3.5, $A(R)$ and $B(R)$ also absorb any axisymmetric azimuthal deviations from Keplerian and radial velocities, respectively. This means that the warp interpretation is not unique.

A necessary condition for warps to explain velocity structures is evident from Equation (10): $\delta v_{\rm los}$ must have an azimuthal wavenumber of m $= \pm 1$ along a given annulus. In Section 3 we fit indiscriminately for warp structures, but the success of this fit can be understood as the degree to which a disk conforms to this criterion.

2.3. Physical Coordinates

The above is derived entirely in the plane of the sky. It is useful to understand how these observed perturbations connect to physical warping in the disk. We therefore consider the literature definitions of three angles, which are the tilt β, the twist γ, and what we will call in this work the warp amplitude ψ. In Appendix A we define these angles formally and relate them to the perturbations δi and δPA. The convenient small-angle approximations are

$$\beta(R) \approx \sqrt{\delta i(R)^2 + \delta{\rm PA}(R)^2\sin^2 i_0}, \tag{13}$$

$$\gamma(R) \approx \arctan 2(\delta i(R), -\sin i_0\,\delta{\rm PA}(R)) \tag{14}$$

$$\psi(R) = R\sqrt{\left(\frac{\partial i}{\partial R}\right)^2 + \sin^2 i\left(\frac{\partial{\rm PA}}{\partial R}\right)^2}. \tag{15}$$

In order to be able to compare disks, hereafter we will refer to a "tilt amplitude," by which we mean $\beta_{\rm max}$ as defined by the maximum value of $\beta(R)$ for a given disk (for a specific molecular tracer and observational beam size). In the literature, ψ is referred to as a "warp amplitude," and we will follow this nomenclature, although it is strictly a gradient. However, as discussed in Appendix A, the warp coordinates are dependent on the reference coordinate system (see also A. Juhász & S. Facchini 2017). The most physically relevant reference frame is that aligned with the total angular momentum of the

---

[25] We use the `linalg.lstsq` method from NUMPY (C. R. Harris et al. 2020).

[26] The annulus radius R is always understood to be the radial location in the deprojected coordinate system, assumed to be the same as the radius in disk coordinates. Strictly we should deproject differently at each radius and refit the DISCMINER iteratively. However, a posteriori the warp angles are typically $\lesssim 3°$, so expected offsets are much smaller than the beam size. We experimented by refitting the disk in newly deprojected coordinates to find very minor differences in the inferred warp structure.

system, as all warped and misaligned structures precess around this axis. However, we note that some numerical studies define the reference frame to be that of a perturbing binary, and, more pertinently in our context, for observed disks we do not know the total angular momentum vector. Care must therefore be taken when comparing the physical coordinates we infer in this work to numerical or analytic models.

3. Results and Discussion

3.1. Case Study: MWC 758

In order to understand how the warp model manifests on the observational properties of disks, it is instructive to explore in detail a single case study before looking at the properties of the broader exoALMA sample. We consider the case of MWC 758, which has famous spirals in scattered light (M. Benisty et al. 2015). Comparing the inclination and position angle in the inner disk inferred with H-band VLTI/PIONIER observations (48° and 100°, respectively; B. Lazareff et al. 2017) to the continuum-derived values (7° and 76°, respectively; P. Curone et al. 2025) also suggests substantial misalignment. It also has a clear $m = 1$ spiral in the LOS kinematic residuals (this structure will be discussed further by M. Fukagawa et al. 2025, in preparation). We consider here how the warping model may explain this spiral, as well as the consequences for other observational diagnostics.

3.1.1. Kinematic Warp Model Outcome

We show the radial profiles for perturbations in inclination δi and position angle δPA in Figure 1. The data points and error bars are from the annuli fitting procedure discussed in Section 2, while the black line shows the mean of a Gaussian process (GP) fit[27] used to interpolate between these points and estimate uncertainties. We adopt a Matern kernel with smoothness parameter $\nu = 2.5$ and initiate the length scale at two beam sizes. We sample LOS velocities every half beam size. Fitting the profiles with a GP has the advantage of (a) establishing uncertainties in our warp metrics by drawing samples from posteriors and (b) calculating the numerical derivatives required to quantify the warp amplitude ψ.

Although annuli are fit independently, we find that a coherent, near-sinusoidal structure emerges in perturbation space, with a similar structure in both inclination and position angle. We also visualize the LOS velocity structure of the ^{12}CO surface for MWC 758 (left), compared to the warped model from our GP fit (right). The total tilt amplitude is $\beta_{\max} \approx 1\overset{\circ}{.}6 \pm 0\overset{\circ}{.}2$. The fits become uncertain in the outer disk region (∼200–250 au), where the data cannot be reproduced by a warp (i.e., δi and δPA become consistent with zero with large uncertainties). In terms of our twisting parameter γ, the twist is a continuous, almost linear (periodic) function of radius. This is what gives rise to clear spiral structure, which becomes apparent when a substantial twist is present. Without a twist, the velocity pattern may alternate between red and blue with increasing radius at fixed azimuth, as with several examples discussed in Section 3.2. The warp amplitude for MWC 758 is approximately constant with radius, with $\psi \sim 0.1$. While this comes close to the analytic criterion for disk tearing (S. Doğan et al. 2018), most numerical studies do not find tearing for small tilt amplitudes ($\beta_{\max} \ll H/R$) that we report here.

As discussed in Section 3.5, the warp can only produce features that have $m = 1$ periodicity on the annulus. In the outer region the velocities around the annuli are offset from the systemic velocity, rather than symmetric. In this case, the velocity field could be the result of a wind (this will be assessed in future exoALMA publications; M. Benisty et al. 2025, in preparation), while variations in emission height (which we do not estimate here) and/or sloshing motions may also contribute to differences. However, within ∼200 au the warp model does reproduce a spiral pattern strikingly similar to the residuals from the Keplerian rotation curve observed in MWC 758. The coherence of the inferred warp structure is further circumstantial evidence in support of this interpretation.

3.1.2. Scattered Light Spirals

Given that warping can evidently generate spiral structure, we can further ask whether it might play a role in generating the spiral arms seen in scattered light (M. Benisty et al. 2015; B. B. Ren et al. 2023; R. Orihara & M. Momose 2025). We therefore run a RADMC3D[28] (C. P. Dullemond et al. 2012) radiative transfer simulation to explore this. We impose a midplane density $\rho_{\rm mid} = \rho_0 (R/R_0)^{-1}$, where $R_0 = 10$ au and our inner edge is 5 au. Since we do not consider gas opacity or self-gravity, ρ_0 is unimportant except for the dust, for which we adopt $\rho_0 = 2 \times 10^{-15}$ g cm^{-3}. We assume well-coupled dust in a vertically isothermal disk in hydrostatic equilibrium with a scale height $H(R) = 0.05 (R/R_0)^{1.03}$, corresponding to mild flaring. To be comparable to the extent of the scattered light observations, we truncate at an outer radius of 160 au.

In the range of radii for which we have kinematic constraints, we perturb the orientation of the disk at each inclination to match our profiles, without any other change to the density at a fixed radius. The warp structure is visualized in Figure 2, where a disc composed of midplane annuli have orientations that are perturbed following the inferred warp profile. Unfortunately, at the distance of MWC 758 the velocity map resolution is prohibitive at radii within the scattered light spirals, where the structure is particularly important for producing shadows outside. However, we can in a general sense assess whether inclinations and position angle perturbations similar to those in MWC 758 may produce comparable structures. We do this by extrapolating a reasonable but arbitrary profile inside the region for which we have kinematic constraints (see Appendix B). Here we aim not to reproduce every constraint but to apply a simple model for the outer disk, which is not meant as a "fit." We also miss physics, such as deviations from vertical hydrostatic equilibrium during warp propagation. Overall, the aim to reproduce the entire system would be a considerable effort beyond the scope of this work. Through our experiment we simply aim to answer the following question: "Can warping produce spiral arm structures in scattered light observations?"

For scattering opacity, we adopt amorphous olivine with equal parts Mg and Fe and optical constants from C. Jaeger et al. (1994) and J. Dorschner et al. (1995) assuming 0.1 μm dust. The stellar spectrum is blackbody, with stellar radius

---

[27] To fit, we use the `GaussianProcessRegressor` of SCIKIT-LEARN (F. Pedregosa et al. 2011), available from https://scikit-learn.org/stable/modules/generated/sklearn.gaussian_process.GaussianProcessRegressor.html.

[28] https://github.com/dullemond/radmc3d-2.0

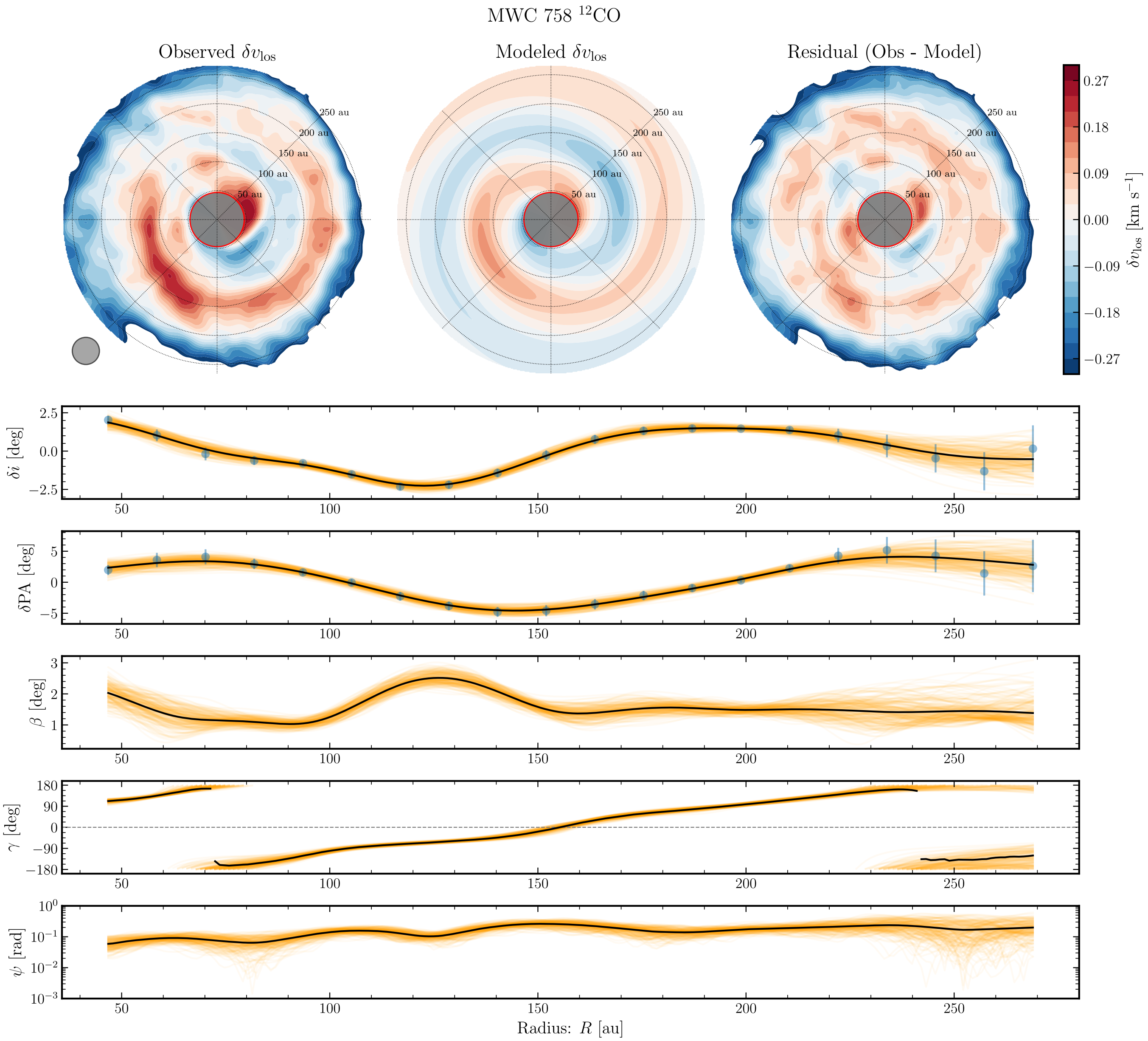

Figure 1. The top panels show residuals from the observed (left) and modeled (middle) $\delta v_{\rm los}$ fields for the source after subtracting Keplerian velocity profiles. The top right panel shows the residual when subtracting the model from the observed velocities. The flexible model is for a simple warped disk geometry, with perturbation in inclination and position angle. The color scale is the LOS velocity in km s^{-1}. Gray circles mask two times the central beam size. The beam size is also shown on the left-hand side, assumed circular for visualization. The lower panels show radial profiles of δi, δPA, and the physical warp properties tilt β, twist γ, and the warp amplitude ψ for MWC 758 from our fitting procedure. Blue points and error bars in δi and δPA come from the least-squares fitting procedure. Faint orange lines show posterior distributions from the GP model.

(The complete figure set (30 images) is available in the online article.)

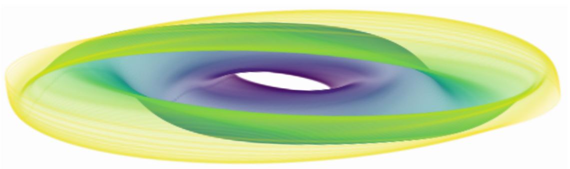

Figure 2. Visualization of the warp structure via concentric rings with the profile for MWC 758 shown in Figure 1. The coordinate system is chosen such that the disk lies in the x–y plane on average, and the z-axis is stretched by a factor four to emphasize the warp. The disk is then viewed slightly from above.

2 $R_\odot$ (although geometrically we assume a point source) and effective temperature 7600 K. The total intensity from the radiative transfer calculation at 2.2 μm is shown in Figure 3, compared to the total polarized intensity as observed with Very Large Telescope (VLT)/SPHERE in the K band (B. B. Ren et al. 2023). The structure is somewhat larger in scale and less sharp than observed. We do not clearly obtain a spiral arm stretching north; it is possible that the visibility of this spiral arm is strongly dependent on flaring angle, breathing motion, or inner disk structure. In Section 3.1.3, we also discuss how emission from close to the midplane may plausibly produce $m = 2$ structures. However, given the simplicity of our model, it is remarkable that we qualitatively reproduce several aspects of the observed structure. Both a long spiral arm stretching south and an overbrightness in the east are visible. In the future, combining tailored reconstruction of the shadowing in scattered light, as performed by

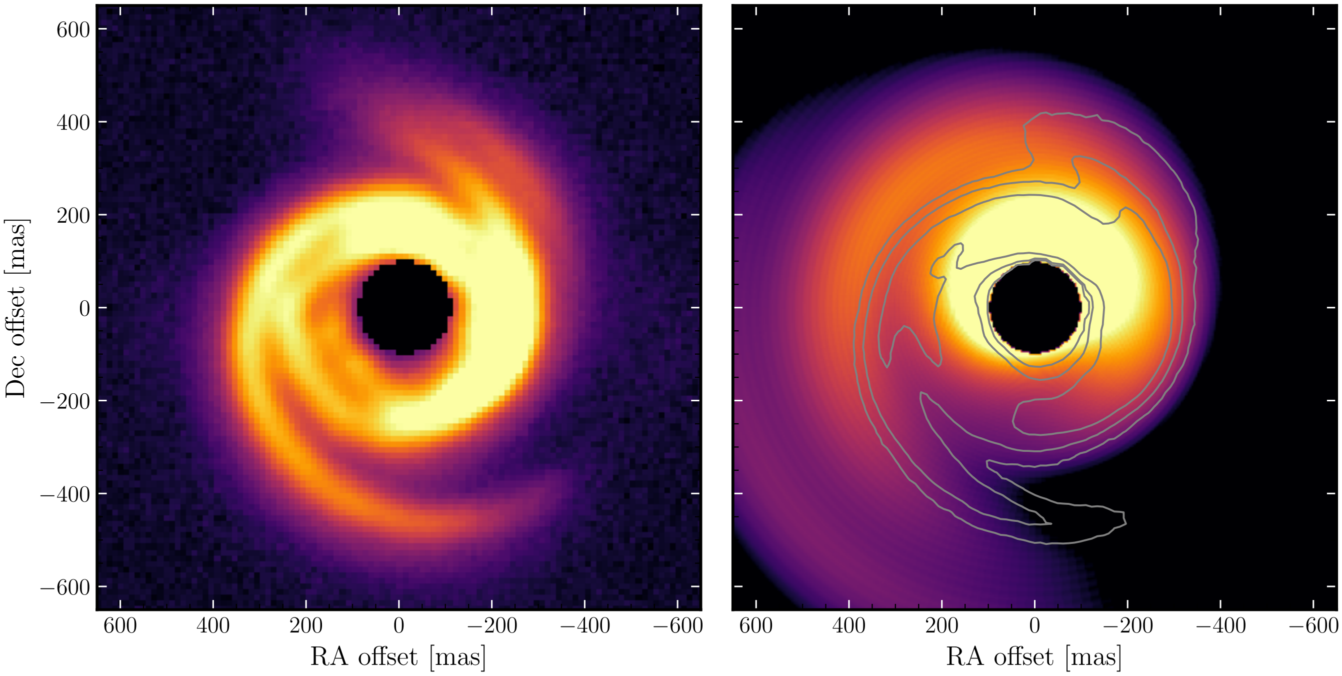

Figure 3. The total K-band polarized intensity map of MWC 758 (left; B. B. Ren et al. 2023) compared to the total intensity at 2.2 μm from our RADMC3D model (right). Both are masked inside 100 mas, which is the size of the coronagraph. The contours of the right panel are 5σ, 10σ, 20σ, and 50σ from the observed structure. We highlight that we do not have good constraints on warp structure inside of 150 mas, where we have assumed a profile with comparable amplitude to the warp farther out (see Appendix B).

R. Orihara & M. Momose (2025), with kinematic modeling may produce a global picture of the disk geometry. Here we simply conclude that the warps required to give the observed signatures in kinematic residuals for MWC 758 are also capable of producing spirals in scattered light.

3.1.3. Brightness Temperature Spirals

MWC 758 shows a spiral structure not only in the LOS kinematic residuals but also in the CO brightness temperature. Based on the thermal structure we infer from our RADMC3D model, we can also explore whether we expect warping to produce similar spirals in brightness temperatures. We might expect some variation in this temperature for the same reason as for the scattered light. Namely, in a warped disk, the surface at the same radius and height above the warped midplane may be irradiated differently depending on the azimuth.

To compare our model to the observed brightness temperature structure, we simply assume that the emission comes from where CO becomes self-shielding (we assume that this vertical column is $N_{\rm ss} = 10^{15}$ cm^{-2}, with depletion with respect to hydrogen of 10^{-6} and a dust-to-gas ratio of 10^{-2}, but our results do not strongly depend on these parameters). We show the result compared to the observations in Figure 4. As for the scattered light model, there are some differences in the tightness of the spirals and the intensity of the structures. However, again, our model does well given its simplicity and lack of detailed physics. Numerous observational effects, as well as physical effects, such as varying flaring angles and photochemistry, may influence the structure (A. K. Young et al. 2021). Indeed, if the vertical motions in the outer disk are tracing a (thermal) wind, then this material could be expected to experience some temperature enhancement. Overall it is clear that warping is capable of producing structures comparable to what we observe.

Finally, we note that it is simple to understand that the brightness temperature structure in the midplane of a warped disk must have $m = 2$ symmetry if there are no other factors. We confirm this in the right panel of Figure 4. In this case, the temperature deviations for the axisymmetric power law are much smaller, but the morphology somewhat better resembles the inner regions of MWC 758. This might hint that the ^{12}CO emission is coming from deeper in the disk than we assume, for example, due to greater photodissociation in the surface layers. This may be the subject of focused experimentation in future work.

3.2. Full exoALMA Sample

We now consider more briefly the remainder of the exoALMA sample. The full sample is discussed in Appendix C, with supporting figures available online. We will discuss in Section 3.2.4 that cases where the back side of the disk is visible in the emission-line profile are problematic. In these cases, the residuals have been extracted from a Keplerian model fitting the double bell line profile using DISCMINER (A. F. Izquierdo et al. 2025), and we highlight these cases below. We still report the warp structures for these disks (summarized in Table 1), but we exclude them from our population level analysis in Section 3.3. We highlight that, even without our analysis, many of the kinematic structures seen in the LOS velocity residuals show arcs and asymmetric features qualitatively similar to those found by A. K. Young et al. (2022) in their numerical simulations of warped disks.

3.2.1. Strong Warping Candidates

Alongside MWC 758, the LOS residuals for disks around CQ Tau are one of the most striking examples of a spiral structure that can be described well by coherent, twisted spirals

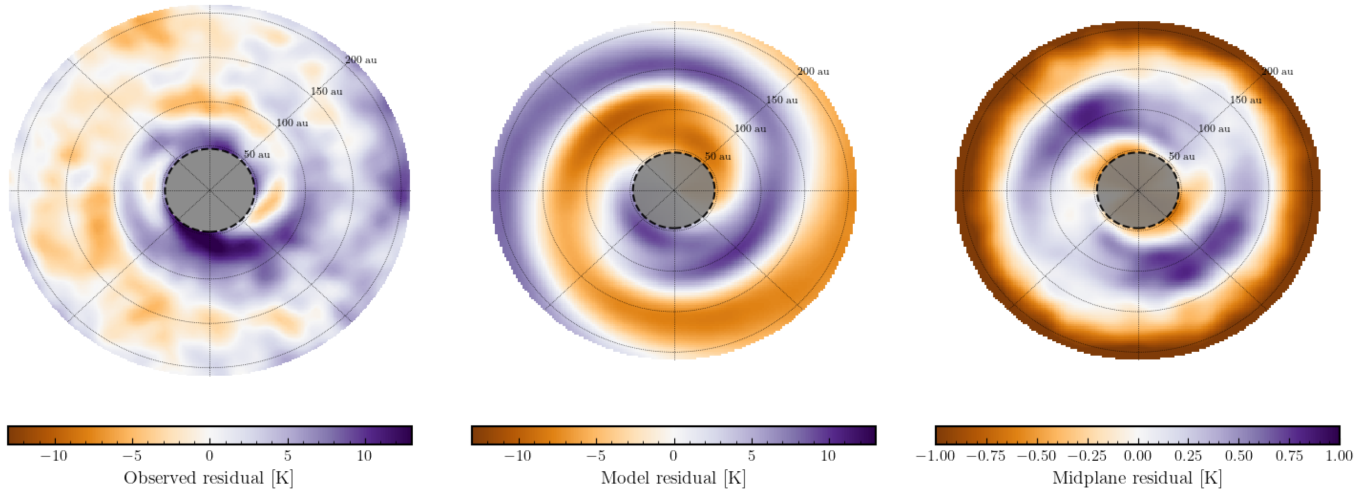

Figure 4. Residual brightness temperature of ^{12}CO after subtracting an axisymmetric power law as observed in MWC 758 (left) and our warped disk model at an estimated CO emission height (middle) and midplane from the model (right). The temperature quoted in each case is the difference from a fitted radial axisymmetric power-law model. The model has been smoothed over a circular beam for visualization purposes, assuming zero temperature residual outside of the simulated range. The CO surface temperature from the model (middle) broadly matches the observed structure (left), but the midplane pattern (right) resembles the $m = 2$ symmetry in the inner region.

Table 1
Properties of the Disks in the exoALMA Sample That We Adopt or Derive in This Work

Source	$M_\star$ ($M_\odot$)	i_0 (deg)	$R_{\rm out}$ (au)	δi (deg)	δPA (deg)	$\beta_{\rm max}$ (deg)	$\langle \log \psi \rangle_R$	NAI	Acc. R.[a]	DB?[b]
MWC 758	1.40	19.4	266.6	−2.3 to 2.0	−4.8 to 5.2	2.56±0.17	−0.85±0.03	0.43	−7.15	N
V4046 Sgr	1.73	−33.6	358.2	−0.5 to 0.9	−0.2 to 0.2	0.87±0.02	−1.71±0.03	0.03	−9.30	N
HD 34282	1.62	−58.3	741.6	−5.2 to 8.3	−2.8 to 1.5	7.40±0.33	−0.67±0.04	0.11	−7.70	Y
AA Tau	0.79	−58.7	497.0	−6.6 to 3.4	−1.7 to 1.2	6.21±0.44	−0.79±0.04	0.12	−8.10	Y
CQ Tau	1.40	−36.2	152.0	−2.8 to 2.4	−1.8 to 2.2	2.97±0.27	−0.84±0.03	0.11	−7.00	N
DM Tau	0.45	40.3	535.7	−3.1 to 3.7	−2.1 to 1.3	3.60±0.19	−0.97±0.04	0.09	−8.20	Y
HD 135344B	1.61	−16.1	222.8	−1.1 to 1.2	−2.7 to 4.2	1.60±0.14	−1.26±0.04	0.41	−8.00	N
HD 143006	1.56	−16.9	170.6	−0.3 to 1.1	−1.6 to 1.4	1.14±0.07	−1.40±0.05	0.21	−8.10	N
J1604	1.29	6.0	251.6	−0.6 to 0.4	−1.3 to 2.2	0.61±0.04	−1.62±0.04	0.06	−10.50	N
J1615	1.14	46.1	538.2	−3.7 to 3.7	−1.6 to 1.0	3.60±0.13	−1.13±0.03	0.04	−8.50	Y
J1842	1.07	39.4	317.1	−2.2 to 3.7	−1.2 to 1.0	3.56±0.25	−1.33±0.04	0.07	−8.80	Y
J1852	1.03	−32.7	247.0	−2.3 to 1.0	−0.2 to 0.5	1.71±0.22	−1.55±0.04	0.02	−8.70	N
LkCa 15	1.17	50.4	698.0	−5.7 to 4.4	−0.9 to 0.8	5.61±0.14	−0.95±0.03	0.05	−8.40	Y
PDS 66	1.28	−31.9	132.2	−1.1 to 1.1	−1.6 to 0.3	1.44±0.14	−1.51±0.03	0.01	−9.90	N
SY Cha	0.81	−50.7	535.1	−6.2 to 10.5	−5.2 to 0.9	10.17±0.52	−0.73±0.03	0.07	−9.20	Y

Notes. For the δi and δPA values we report the total range resulting from our fitting procedure. For $\beta_{\rm max}$ we quote the $\pm 1\sigma$ uncertainty. Stellar masses M_* and outer radii $R_{\rm out}$ are from the DISCMINER fitting procedure (A. F. Izquierdo et al. 2025), and the NAIs for the continuum are from P. Curone et al. (2025). Stellar accretion rates $\dot{M}_{\rm acc}$ are mostly the same as those adopted by P. Curone et al. (2025), with the following references: AA Tau—J. Bouvier et al. (2013); CQ Tau—B. Donehew & S. Brittain (2011); DM Tau, J1615, J1842, J1852, LkCa 15—C. F. Manara et al. (2014); J1604—A. Sicilia-Aguilar et al. (2020); HD 135344B—M. L. Sitko et al. (2012); HD 143006—E. Rigliaco et al. (2015); HD 34282—J. R. Fairlamb et al. (2015); MWC 758—N. Huélamo et al. (2018); PDS 66—L. Ingleby et al. (2013); SY Cha—C. F. Manara et al. (2023); V4046 Sgr—J. F. Donati et al. (2011).

[a] Accretion rate: $\log \dot{M}_{\rm acc}$ [$M_\odot$ yr^{-1}].

[b] Double bell used to fit line profiles—i.e., visible back side.

with nonconstant $\gamma(R)$. Intriguingly, these two cases are also those for which SO, a putative shock tracer (N. Sakai et al. 2014), has been detected (F. Zagaria et al. 2025). Speculatively, rapid “sloshing” motions produced by the warp may drive shock heating in these cases (e.g., C. N. Kimmig & C. P. Dullemond 2024; see also Section 3.4).

In addition to MWC 758 and CQ Tau, the disks around HD 135344B, HD 143006, and J1604 all exhibit a similarly spiral-like structure in at least part of the disk. They also have substantial variations in position angle, which would require potentially contrived combinations of radial and azimuthal velocity variations to produce similar LOS signatures by axisymmetric perturbations. Most of these disks also have strong evidence of warping uncovered by previous studies, as discussed in Appendix C. We therefore suggest that these cases represent some of the clearest warped disk candidates, although this precludes neither alternative explanations in these cases nor the warping hypothesis in the remaining exoALMA sample.

3.2.2. Ambiguous Structure

While the warp model has success in reproducing LOS residuals in several disks, some of the structures we attribute to the warp may be more readily explained in alternative ways. In particular, cases for which we see a systematic blue−red trend across the major axis can be interpreted as slower than Keplerian rotation owing to radial pressure gradients (C. Longarini et al. 2025; J. Stadler et al. 2025).

It is not possible to unambiguously distinguish between pressure gradients and warping. However, regions of the outer disk where the apparent δPA is consistent with zero would require a coincidence of viewing angle if they are warped, making pressure gradients a more compelling explanation. Most of the disks have at least some outer structure that can be interpreted in this way. In fact, physically we expect all disks to exhibit this feature; it is even possible that a disk warp has obscured this feature in cases where we do not see it clearly.

We do not attempt to distinguish directly which parts of the assumed warp structure may be due to pressure gradients. However, from visual inspection some examples where substantial pressure-related residuals may lead to warp amplitude overestimation include HD 34282, LkCa 15, PDS 66, SY Cha, and V4046 Sgr.

3.2.3. Interpreting Residuals

Residuals include some $m = 2$ structures, some of which switch signs along major and minor axes. Such structures might be readily explained by small errors in the geometric center or the emission surface height (this will be assessed by M. Fukagawa et al. 2025, in preparation). Since DISCMINER fits these parameters for a nonwarped disk model, future modifications that incorporate the warp might improve these residual features. In the context of this work, the expected errors in geometric fitting parameters should not greatly influence the warp structure we infer. The $m = 2$ structures are not fit by the $m = 1$ warp, and uncertainties in a global PA and inclination would just result in approximately constant β and γ values, with small ψ throughout the disk.[29] We therefore expect our warp metrics to be robust against these uncertainties, while accounting for the putative warp may improve residual extraction in the future.

We also find that for some of the disks, including J1604, SY Cha, and MWC 758, once extracting off the warp we find $m = 0$ structures in the form of systematically redshifted residuals in the inner region and blueshifted residuals in the outer region, suggestive of a wind. It is possible in these cases that small uncertainties in the systemic velocity mean that the inner disk is actually at the systematic velocity, while the outer disk is somewhat more blueshifted than assumed. Whether or not this can be interpreted as a wind will be discussed in a coming exoALMA paper (M. Benisty et al. 2025, in preparation).

3.2.4. Highly Inclined Disks and Back-side Emission

HD 34282, AA Tau, DM Tau, J1615, J1842, LkCa 15, and SY Cha are high-inclination disks, where the back side is visible (for which double bell line profiles were applied in tomographic analysis; A. F. Izquierdo et al. 2025). These disks have systematically larger tilt amplitudes. We show the distribution of amplitudes in PA and inclination in Figure 5, where this is evident. There are two obvious possible explanations for this finding. One explanation is that the noisy structure could simply trick the fitting procedure into adopting different inclinations (although in principle our GP modeling should automatically account for noise in fitting an $m = 1$ structure).

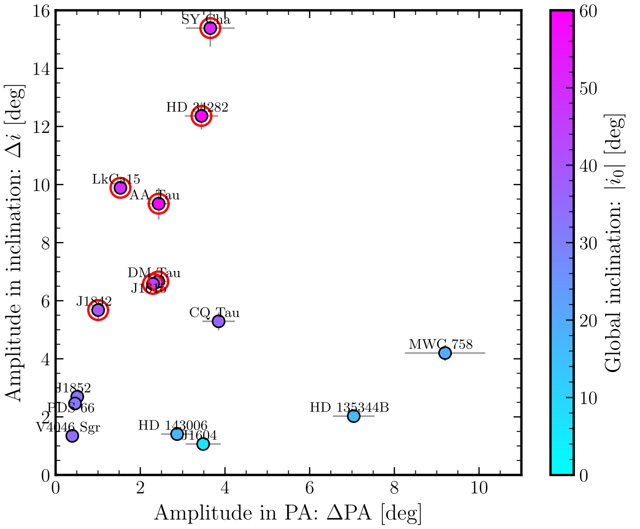

Figure 5. The relationship between inclination and PA tilt amplitude, with points being colored by overall inclination of the system. The points circled in red are those for which the back side of the disk is visible in the ^{12}CO line profiles.

A second plausible scenario is that there are substantial radial motions that have a greater LOS component in these high-inclination disks. We have already discussed in Section 3.2.2 how are fitting procedure might attribute radial winds to warping. Alternatively, if the structures really are due to warps, then the high-inclination disks may catch more of the radial sloshing motions that can contribute significantly to the LOS velocity residuals at high inclination, as discussed in Section 3.4, although we do not find a strong emission height dependence (see Section 3.2.5). Radial sloshing combined with the back-side contribution could provide an explanation for the difficulties in fitting the simple Keplerian models in these cases. This phenomenon warrants future exploration, but for now we note that the warp properties are probably not reliably inferred in these high-inclination cases. We therefore exclude them from our analysis in Section 3.3.

3.2.5. Emission Height Dependence

One of our assumptions in applying the warp model is that the dominant contribution to the LOS velocity perturbations is azimuthal velocity in the natural coordinate system of a given annulus. However, the molecular emission surface for ^{12}CO is in fact substantially above the midplane (M. Galloway-Sprietsma et al. 2025), where we might expect more complex kinematics of the warp structure. We can estimate the sensitivity of our results to the finite emission height by repeating our experiment for isotopologues with a lower optical depth, emitting from lower down in the disk.

In Figure 6, we show the dependence of $\beta_{\max}$ on the choice of isotopologue. We recover very similar tilt amplitudes for both ^{12}CO and ^{13}CO. The ^{13}CO systematically exhibits a slightly lower $\beta_{\max}$, which might be the result of lower sensitivity in the outer disk, truncating the region over which we can fit the warp model. For disks that have been imaged at the larger beam size of $0\farcs3$, we checked the dependence of our

---

[29] We have validated this by offsetting parameters for synthetic DISCMINER models.

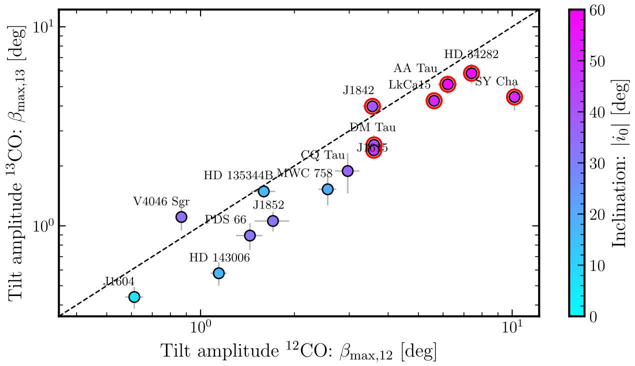

Figure 6. Comparison between the tilt amplitudes inferred using ^{12}CO and ^{13}CO isotopologues. The black dashed line shows 1:1 agreement. Points are colored by the global inclination of the disk. The disks for which the back side is visible in the line profiles are circled in red.

results on resolution. We found in these cases good agreement in ^{12}CO and agreement in ^{13}CO except for the cases DM Tau, SY Cha, and HD 34282, which show discrepancies for β_{max} of 2°–3°. The latter are all disks with a visible back side, which we exclude from our statistical analysis in Section 3.3. We conclude that our results, particularly for low-inclination disks, are robust to the observational tracer and resolution. We emphasize that while this constitutes evidence that we are not biasing our warp fit by motions that are localized vertically or radially, this does not necessarily validate the warp interpretation.

3.3. Correlations with System Properties

We now restrict our consideration to exoALMA disks with moderate inclinations, for which the back-side emission is not visible, in order to search for correlations between the warp and system properties. In Figure 7 we show how the amplitude of the warp β_{max} correlates with nonaxisymmetric structure in the dust (measured via the nonaxisymmetric index (NAI); P. Curone et al. 2025); stellar accretion rate and stellar accretion rate normalized by the square of the stellar mass, the latter being the approximate observed scaling (e.g., C. F. Manara et al. 2017; V. Almendros-Abad et al. 2024; L. Delfini et al. 2025); and the NIR excess (A. Garufi et al. 2018). We perform Spearman, Kendall τ, and permutation statistical tests in each case. We implement the permutation test by comparing the correlation coefficient $r_{xy} = \sigma_{xy}/\sqrt{\sigma_{xx}\sigma_{yy}}$, where σ_{xy} is the covariance between x and y, over 10^4 permutations.

We do not find any correlation between β_{max} and the NAI, nor do we find a correlation with the NIR excess (A. Garufi et al. 2018). This would perhaps be unsurprising given that the continuum and NIR emission is far more compact than the large-scale gas structures. However, by this same logic we would also not necessarily expect to see a correlation between stellar accretion rate and tilt amplitude. Interestingly, though, we do find marginally significant correlations with accretion rates among our cleaned sample, although our sample size is small.

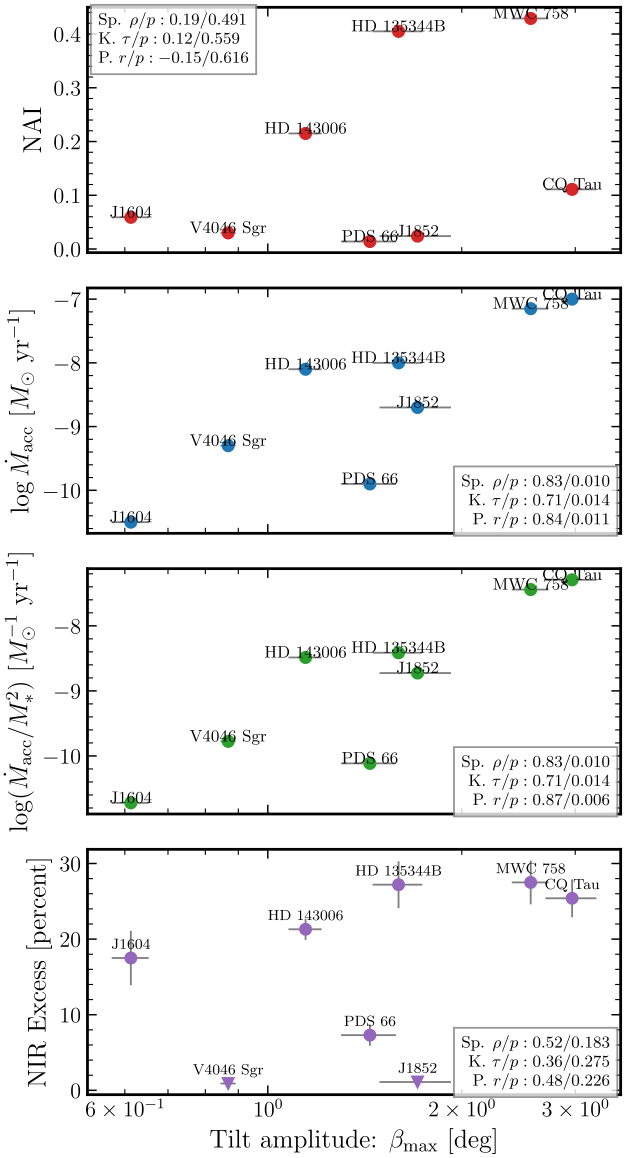

Figure 7. From top to bottom, we show how the the continuum NAI (top panel; P. Curone et al. 2025), stellar accretion rates (second panel from top), normalized stellar accretion rates (to the square of the stellar mass; third panel), and NIR excess (A. Garufi et al. 2018; bottom panel) depend on the range of tilt amplitudes we infer from our model. The outcomes of Spearman rank, Kendall τ, and permutation correlation tests are shown in terms of correlation statistic and p-value. We exclude cases where inclination is unfavorable owing to the appearance of the back side of the disk.

Arguably a more appropriate quantity is the warp amplitude ψ, which encodes within it the dynamical stability of the warp (S. Doğan et al. 2018). If ψ is large, annuli may split. It is not necessarily clear without more detailed calculation whether a high ψ would result in permanent tearing of the disk or some instability followed by reconnection of the annuli back into a continuous disk—this may depend on the equation of state (H. Deng & G. I. Ogilvie 2022). Even if a disk is stable, angular momentum transport inward would still be facilitated by damping of the warp, since the sum of the angular momentum vectors of neighboring annuli must result in contraction when the disk returns to the plane (e.g., G. Lodato & J. E. Pringle 2006). If we assume that what matters for accretion is a global enhancement of ψ across all radii, then we can define a geometrically averaged quantity:

$$\langle \log \psi \rangle_R = \frac{1}{\Delta R} \int \log \psi \, dR, \tag{16}$$

where ΔR is the range of radii over which we integrate. This statistic has the benefit that it should not be strongly dependent

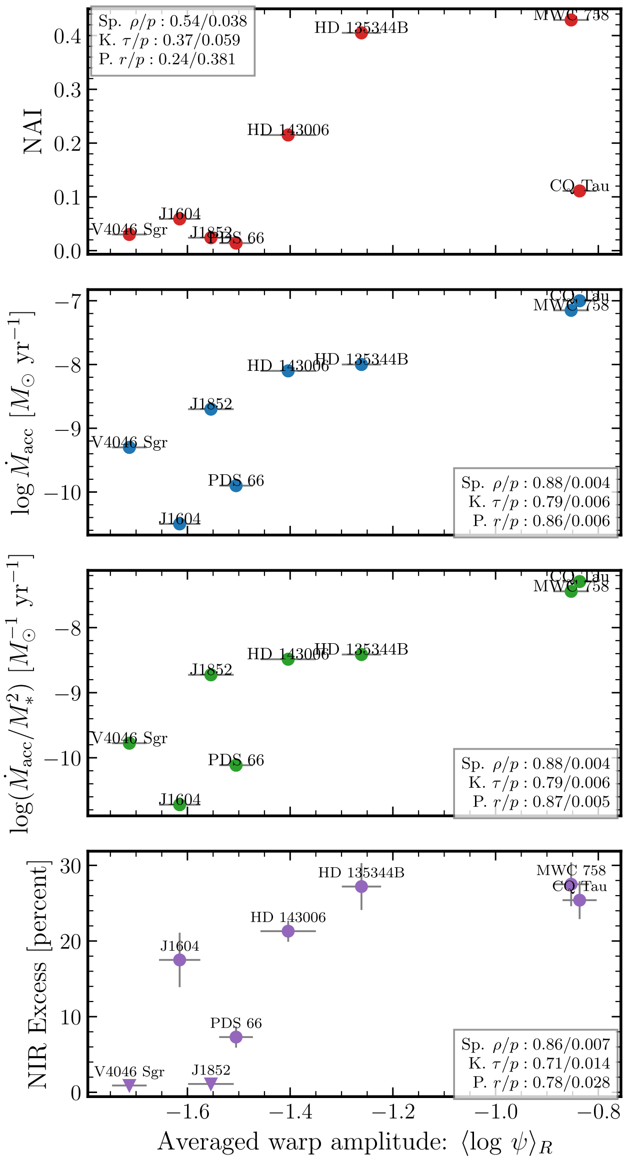

Figure 8. Same as Figure 7, but with the averaged logarithmic warp amplitude for the sample of exoALMA disks on the x-axis. Results of statistical correlation tests are shown as in Figure 7.

on local noise, but rather is a metric of whether we find high values persistently through the disk.

The star and disk properties as a function of $\langle \log \psi \rangle_R$ are shown in Figure 8. In this case, we find at least marginally significant correlations in all four cases for the majority of statistical tests. Despite the small sample size, we obtain p-values down to $p \approx 4 \times 10^{-3}$ (2.7σ). These correlations appear compelling if not categorical; expanding the sample size remains a goal for the future.

Perhaps from an empirical point of view we should no longer be surprised; we have hypothesized that warping may contribute to scattered light spiral structures, and it has previously been shown that these spirals are correlated with NIR excess in the inner disk (A. Garufi et al. 2018). Nonetheless, this new correlation raises the exciting prospect that warps themselves may be responsible, in whole or in part, for angular momentum transport through the outer disk. If late-stage infall is a driver of the disk warping, this may connect to the recently reported correlations between local interstellar medium density and accretion rates (C. Rogers et al. 2024; A. J. Winter et al. 2024a; L. Delfini et al. 2025). Clearly the sample size is small, and further work is needed to verify the correlation and explore the connection to infall.

3.4. Caveats for the Simple Model

3.4.1. Warp Propagation

The first caveat for our simple model is that we have ignored the contribution to the velocity field from the propagation of the warp through the disk. We can estimate the amplitude of the nonazimuthal motions due to this propagation by noting that the period of oscillation for the warp in the bending regime is

$$P_{\rm warp} \approx \frac{R}{c_s}. \tag{17}$$

Equation (17) comes from the fact that the warp wave speed is $c_s/2$ and the bending wavelength is $R/2$ (S. H. Lubow & G. I. Ogilvie 2000). Then, the out-of-plane motion of the disk due to the warp propagation is

$$v_{{\rm warp},z} \sim \beta_{\rm max} R / P_{\rm warp}, \tag{18}$$

where $\beta_{\rm max}$ is the tilt amplitude in radians. If we assume $\beta_{\rm max} = 10^\circ$, we have $v_{{\rm warp},z} \sim 0.17 c_s \sim 0.02 v_\phi$ for $H/R = 0.1$. This is small compared to the expected projected contribution from the perturbed azimuthal velocity and the perturbation required to reproduce LOS variations (J. Stadler et al. 2025).

3.4.2. Sloshing and Breathing

Another approximation is made in assuming throughout our calculation that all motion is in the midplane and azimuthal. This is clearly not the case, with the ^{12}CO surface raised substantially out of the midplane (e.g., M. Galloway-Sprietsma et al. 2025). At these heights, the molecular surfaces of a warped disk may be subject to not only the motions induced by the warp propagation but also so-called "sloshing" and "breathing" motions (e.g., G. Lodato & J. E. Pringle 2007). These motions are produced by pressure gradients due to the vertical offset between annuli, which lead to epicyclic motions that exert a substantial torque on the disk (J. C. B. Papaloizou & J. E. Pringle 1983). In the limit of low tilt amplitude for inviscid disks, these can be divided into the horizontal sloshing (in R and ϕ) and the vertical breathing mode (G. I. Ogilvie & H. N. Latter 2013).

While the exact impacts of each of these contributions are complex, we can make some order-of-magnitude estimates. Starting with the breathing motion, if the molecular emission surface is substantially above the midplane, then we may expect a fluid element to travel a distance of order its average height $\langle z_{\rm surf} \rangle$ over a warp oscillation time. Then, breathing modes would plausibly have velocity

$$v_{\rm breath} \sim \langle z_{\rm surf} \rangle / P_{\rm warp}. \tag{19}$$

If we assume $\langle z_{\rm surf} \rangle = 2H$, for pressure scale height H, we have $v_{{\rm warp},z} \sim 2c_s^2/v_\phi \sim 0.02 v_\phi$. C. N. Kimmig & C. P. Dullemond (2024) find similar breathing motions to our estimate, $\sim 0.2 c_s$. This is also a comparatively small contribution.

G. Lodato & J. E. Pringle (2007) showed that the warp produces a vertically shearing horizontal motion in the (nominal) disk plane in the form $v_{\rm slosh} \sim (\psi/\alpha)\Omega z$. The precise analysis by C. P. Dullemond et al. (2022) confirms this estimate to within factors of order unity and decomposed the r and ϕ components. Taking the real part of their Equations (88) and (89), appropriate in a vertically isothermal, perfectly Keplerian disk, with low viscosity ($\alpha \ll 1$), the amplitude of the sloshing velocities is

$$v_{r,\mathrm{slosh}} \approx \frac{\psi}{2\alpha}\Omega z, \quad v_{\phi,\mathrm{slosh}} \approx \frac{\psi}{4\alpha}\Omega z, \tag{20}$$

where Ω is the angular frequency and z is the height above the midplane. At one pressure scale height, $z_{\mathrm{surf}} = H$, the maximum sloshing velocity is $v_{\max} = \psi c_s/(2\alpha)$, which gives $\sim 5c_s$ for $\psi = 10^{-2}$ and $\alpha = 10^{-3}$. In their simulations, C. N. Kimmig & C. P. Dullemond (2024) indeed find radial sloshing velocities on that order of magnitude.

If these sloshing motions are indeed several times the sound speed, then they will undoubtedly contribute to the LOS velocity structures. However, we note that at altitudes $z_{\mathrm{surf}} \gtrsim H$ the assumptions taken to estimate the sloshing motions break down, as the vertical communication timescale becomes longer than the orbital timescale. Shocks are likely to occur, which produce a complicated velocity field and might influence the thermal structure at the disk surfaces. We expect both shocks and instabilities also for $\psi \gg \alpha$ (see, e.g., S. Doğan et al. 2018). This could lead to rapid decay of the warp, and therefore large sloshing velocities may require a persistent driving torque to be sustained.

For the purposes of this work, we note that in cases where sloshing motions are prevalent this may be expected to break the $m = 1$ symmetry to which we fit our warp model, since $m = 1$ in r and ϕ velocity components follows from axisymmetric motions on the annulus. We might then expect this to manifest as noise in our fitting procedure. We can test this indirectly. Given that sloshing motions should be vertically and radially dependent, if they strongly influence our results, we may expect substantial tilt amplitude differences depending on the spatial region probed. We explore the effects of varying molecular tracer (i.e., z_{surf}) and beam size (see discussion in Section 3.2.5). We find that our results remain broadly unchanged. This does not prove that sloshing motions are not present, but it suggests that they might act more like noise than a strong bias. This clearly still requires investigation in future work, including the role of shock dissipation and how the emission height changes under their influence (M. Galloway-Sprietsma et al. 2025), and this should be understood as a caveat of our results.

3.4.3. Optical Depth

A. K. Young et al. (2022) demonstrated in their numerical calculations that the optical depth of the molecular tracer can have a substantial effect on the inferred warp properties, due to the contribution to emission from different parts of the column along the LOS. This is shown particularly in their Figure 7, where the expected difference in the inferred phase angle is often tens of degrees between ^{12}CO and ^{13}CO (assuming a factor ∼10 difference in optical depth). Interestingly, we do not see a substantial difference between ^{12}CO and ^{13}CO, at least in the maximal tilt angle we infer, with minor systematic differences of typically $<1^\circ$ as discussed in Section 3.2.5. Unraveling the dependence of warp structure on optical depth will certainly require an effort to produce synthetic observables for specific disks. We also highlight that our inferred tilt profiles for disks such as MWC 758 and CQ Tau have an approximately linear twist profile with radius, which does not resemble the twist profile expected around circumbinary disks (e.g., G. Lodato & S. Facchini 2013), as modeled by A. K. Young et al. (2022). This might indicate that in some cases at least the warp is not driven by a binary. This could have further ramifications for comparisons to numerical models and synthetic observations. We leave a full physical model and radiative transfer calculations tailored to specific disks to future work, for which our warp profile fits offer a starting point.

3.5. Nonuniqueness of the Warping Interpretation

We emphasize that in the literature to date the LOS velocity residuals have typically (although not always) been interpreted as planar axisymmetric structures (e.g., J. Stadler et al. 2025), winds (e.g., T. J. Haworth et al. 2017; M. Benisty et al. 2025, in preparation), spiral arms (e.g., R. Teague et al. 2022; B. B. Ren et al. 2024), laminar flows (e.g., K. A. Rosenfeld et al. 2014; A. Zuleta et al. 2024), or localized perturbations such as those due to planets (e.g., C. Pinte et al. 2018, 2020). The warp model we discuss in this Letter cannot explain any kind of feature in kinematics without azimuthal wavenumber $m = 1$, although, as we show in this work, this may produce diverse structures in other tracers. Residual features after subtraction of the warp model include winds that are predominantly vertical and localized structures.

The warp model is also degenerate with azimuthally symmetric perturbations in the radial and azimuthal components, which are both $m = 1$ in their LOS component (e.g., A. F. Izquierdo et al. 2021). This means that features driven by processes such as pressure support or self-gravity may also explain some of the observed structures (e.g., G. Lodato et al. 2023; P. Martire et al. 2024; B. Veronesi et al. 2024; C. Longarini et al. 2025). Although these planar, axisymmetric models may need to be somewhat contrived to produce some of the spiral-like structures found in LOS kinematics, the warp interpretation is not unique. In principle, with detailed physical and radiative transfer modeling, it may be possible to distinguish the warp from other kinds of kinematic perturbation. However, this is not the goal of this work, which is instead meant to offer an alternative explanation for the large-scale structures seen across the exoALMA sample. We have shown that the success, simplicity, and potential to explain a range of observational evidence are all arguments in favor of the warp interpretation. Nonetheless, our results should be understood as a challenge to the assumption that disks are planar and as an upper limit on disk warping in the sense that we attribute $m = 1$ structures as far as possible to the warp. We do not claim that all large-scale kinematic perturbations are the result of warps.

4. Conclusions

We have shown that much of the large-scale structure in the exoALMA sample is consistent with a warped disk. Moderate-amplitude warps with $\Delta\beta \sim 0\overset{\circ}{.}5$–$2^\circ$ can reproduce the main features in several LOS kinematic residuals from a Keplerian model if these residual features have point antisymmetry and satisfy $m = 1$ periodicity on the annulus. Alongside other models, warping is not a unique interpretation for the observed LOS residuals. However, for disks where the large-scale kinematic structure has $m = 1$ symmetry warping is a compelling and simple model that may be understood as a benchmark with which to compare competing physical models. It also fits with growing evidence that warping and misalignment are common occurrences among protoplanetary disks (A. M. Cody et al. 2014; A. Garufi et al. 2018; M. Benisty et al. 2023). The warp interpretation also appears to be a promising way to explain the scattered light and CO brightness temperature morphology of MWC 758 and possibly other disks with prominent spirals.

Assuming that a warp structure explains a large part of observed $m = 1$ kinematic substructure, we explored possible correlations of warping with departures from symmetry in the continuum, stellar accretion rates, and NIR excess. In particular, we considered both the magnitude of the tilt and the geometrically averaged warp amplitude. We find a positive correlation only with stellar accretion for the magnitude of the tilt, but with all of the disk properties (to varying degrees of significance) for the geometrically averaged warp amplitude. The sample size should be increased in future work to confirm these correlations. Nonetheless, our results add to the growing evidence for communication between the inner and outer disks and hint at a potential role of large-scale perturbations in driving stellar accretion.

We conclude that warps and their physical drivers should be explored alongside alternative mechanisms as a plausible pathway to produce large-scale kinematic structures.

Acknowledgments

We thank the anonymous referee for the close reading and useful comments and Kees Dullemond for helpful discussion and insights into the dynamics of warped disks. A.J.W. has been supported by the European Union's Horizon 2020 research and innovation program Marie Skłodowska-Curie grant agreement No. 101104656 and by the Royal Society through University Research Fellowship grant No. URF\R1\241791. M.B., J.S., and D.F. have received funding from the European Research Council (ERC) under the European Union's Horizon 2020 research and innovation program (PROTOPLANETS, grant agreement No. 101002188). Support for A.F.I. was provided by NASA through NASA Hubble Fellowship grant No. HST-HF2-51532.001-A awarded by the Space Telescope Science Institute, which is operated by the Association of Universities for Research in Astronomy, Inc., for NASA, under contract NAS5-26555. G.L. and C.L. have received funding from the European Union's Horizon 2020 research and innovation program under Marie Sklodowska-Curie grant agreement No. 823823 (DUSTBUSTERS). G.L. acknowledges support from PRIN-MUR 20228JPA3A and from the European Union Next Generation EU, CUP:G53D23000870006. G.R. and C.K. acknowledge support from the European Union (ERC Starting Grant DiscEvol, project No. 101039651) and from Fondazione Cariplo, grant No. 2022-1217. J.B. acknowledges support from NASA XRP grant No. 80NSSC23K1312. N.C. has received funding from the European Research Council (ERC) under the European Union Horizon Europe research and innovation program (grant agreement No. 101042275, project Stellar-MADE). P.C. acknowledges support by the Italian Ministero dell'Istruzione, Università e Ricerca through the grant Progetti Premiali 2012—iALMA (CUP C52I13000140001) and by the ANID BASAL project FB210003. S.F. is funded by the European Union (ERC, UNVEIL, 101076613). S.F. acknowledges financial contribution from PRIN-MUR 2022YP5ACE. M.F. is supported by a grant-in-aid from the Japan Society for the Promotion of Science (KAKENHI: No. JP22H01274). C.H. acknowledges support from NSF AAG grant No. A. T.H. is supported by an Australian Government Research Training Program (RTP) Scholarship. J.D.I. acknowledges support from an STFC Ernest Rutherford Fellowship (ST/W004119/1) and a University Academic Fellowship from the University of Leeds. C.L. has received funding from the UK Science and Technology research Council (STFC) via the consolidated grant ST/W000997/1. F.M. has received funding from the European Research Council (ERC) under the European Union's Horizon Europe research and innovation program (grant agreement No. 101053020, project Dust2Planets). C.P. acknowledges Australian Research Council funding via FT170100040, DP18010423, DP220103767, and DP240103290. H.-W.Y. acknowledges support from National Science and Technology Council (NSTC) in Taiwan through grant NSTC 113-2112-M-001-035 and from the Academia Sinica Career Development Award (AS-CDA-111-M03). T.C.Y. acknowledges support by grant-in-aid for JSPS Fellows JP23KJ1008. Support for B.Z. was provided by the Brinson Foundation. Views and opinions expressed by ERC-funded scientists are, however, those of the author(s) only and do not necessarily reflect those of the European Union or the European Research Council. Neither the European Union nor the granting authority can be held responsible for them.

This Letter makes use of the following ALMA data: ADS/JAO.ALMA#2021.1.01123.L. ALMA is a partnership of ESO (representing its member states), NSF (USA) and NINS (Japan), together with NRC (Canada), MOST and ASIAA (Taiwan), and KASI (Republic of Korea), in cooperation with the Republic of Chile. The Joint ALMA Observatory is operated by ESO, AUI/NRAO and NAOJ. The National Radio Astronomy Observatory is a facility of the National Science Foundation operated under cooperative agreement by Associated Universities, Inc. We thank the North American ALMA Science Center (NAASC) for their generous support, including providing computing facilities and financial support for student attendance at workshops and publications.

Data Availability

The fitting scripts used in this work are available at https://github.com/ajw278/warpfitter. The Gaussian process posterior samples of warp parameters for the exoALMA protoplanetary disk sample are available in Zenodo at doi: 10.5281/zenodo.15878577.

Appendix A
Physical Warp Properties

In this appendix, we relate physical warp angles to the observational perturbations to which we fit directly. However, it must be understood that these coordinates come with an unavoidable ambiguity. Theoretical studies may choose different frames by which to define the physical warp parameters (e.g., a binary orbit, inner disk, or outer disk), although the most physically relevant is the total angular momentum of the system. These choices have an effect on how the profiles appear, and even on metrics extracted from the warp structure. For example, in Figure 3 of A. Juhász &

S. Facchini (2017) it can be clearly seen that the physical warp angles vary depending on the choice of reference angular momentum vector. In our work, the natural choice for the reference angular momentum unit vector is that of the unperturbed disk geometry fit by DISCMINER (A. F. Izquierdo et al. 2025). There is no perfect choice, and this consideration will become relevant for future theoretical studies aiming to explain warp structure.

A.1. Angular Momentum Vector in the Observed Coordinates

Given a global disk inclination i_0 and position angle PA_0, the unperturbed angular momentum vector in the sky coordinate system is

$$\overrightarrow{l_0} = \begin{pmatrix} -\sin i_0 \sin \mathrm{PA}_0 \\ \sin i_0 \cos \mathrm{PA}_0 \\ \cos i_0 \end{pmatrix}, \tag{A1}$$

where i_0 is the inclination (0° for face-on, 90° for edge-on); PA_0 is the position angle, measured east of north to the redshifted major axis of the disk; and the coordinate system is defined such that x increases to the east, y increases to the north, and z is along the LOS (toward the observer). We now introduce small, radius-dependent perturbations to the inclination and position angle:

$$i(R) = i_0 + \delta i(R), \qquad \mathrm{PA}(R) = \mathrm{PA}_0 + \delta \mathrm{PA}(R),$$

which imply a perturbed unit angular momentum vector of the form

$$\boldsymbol{l}(R) \approx \boldsymbol{l}_0 + \delta i(R)\, \hat{\boldsymbol{e}}_i + \delta \mathrm{PA}(R) \sin i_0\, \hat{\boldsymbol{e}}_{\mathrm{PA}}, \tag{A2}$$

where $\hat{e}_i$ and $\hat{e}_{\mathrm{PA}}$ are local unit vectors on the sphere,

$$\hat{\boldsymbol{e}}_i = \frac{\hat{z} \times \boldsymbol{l}_0}{|\hat{z} \times \boldsymbol{l}_0|}, \tag{A3}$$

$$\hat{\boldsymbol{e}}_{\mathrm{PA}} = \boldsymbol{l}_0 \times \hat{\boldsymbol{e}}_i, \tag{A4}$$

and Equation (A2) is valid for small perturbations $\delta i(R)$ and $\delta\mathrm{PA}(R)$. These define the directions of increasing inclination and increasing position angle on the sphere of possible disk orientations. Note that strictly if $i_0 = 0$ (a face-on disk), then $\boldsymbol{l}_0 = \hat{z}$ and $\hat{z} \times \boldsymbol{l}_0 = 0$—i.e., the unit vectors become undefined when the disk is exactly face-on.

A.2. Disk Coordinates: Tilt and Twist

The orientation of the warped disk at radius R can also be expressed in the disk-aligned frame, where the unperturbed angular momentum vector lies along the z-axis. In this frame, the orientation is defined by two angles: $\beta(R)$, which is the tilt angle away from the z-axis, and $\gamma(R)$, the twist angle about the z-axis. We define the disk-aligned frame $\{\hat{\boldsymbol{e}}_{x'}, \hat{\boldsymbol{e}}_{y}, \hat{\boldsymbol{e}}_{z'}\}$ such that $\hat{\boldsymbol{e}}_{z'}$ is aligned with the unperturbed angular momentum vector $\boldsymbol{l}_0$, which corresponds to inclination i_0 and position angle PA_0. To express $\boldsymbol{l}(R)$ in this frame, we write

$$\boldsymbol{l}(R) = l_{x'}(R)\, \hat{\boldsymbol{e}}_{x'} + l_{y'}(R)\, \hat{\boldsymbol{e}}_{y'} + l_{z'}(R)\, \hat{\boldsymbol{e}}_{z'}, \tag{A5}$$

where

$$l_{x'}(R) = \sin\beta(R) \cos\gamma(R), \tag{A6}$$

$$l_{y'}(R) = \sin\beta(R) \sin\gamma(R) \tag{A7}$$

$$l_{z'}(R) = \cos\beta(R). \tag{A8}$$

To compute these angles from the observed inclination $i(R)$ and position angle $\mathrm{PA}(R)$, we transform the angular momentum vector from the sky coordinates into the disk-aligned frame. This is done by first rotating by $-\mathrm{PA}_0$ about the z-axis, followed by a rotation by $-i_0$ about the x-axis. Rewriting the exact version of Equation (A2), the sky-frame angular momentum vector is given by

$$\boldsymbol{l}(R) = \begin{pmatrix} -\sin i(R) \sin \mathrm{PA}(R) \\ \sin i(R) \cos \mathrm{PA}(R) \\ \cos i(R) \end{pmatrix}. \tag{A9}$$

If we apply a rotation by $-\mathrm{PA}_0$ in the z-axis, followed by $-i_0$ in the x-axis, then we find that the disk-frame components are

$$l_{x'}(R) = -\sin i(R) \sin(\mathrm{PA}(R) - \mathrm{PA}_0), \tag{A10}$$

$$l_{y'}(R) = \cos i_0 \sin i(R) \cos(\mathrm{PA}(R) - \mathrm{PA}_0) + \sin i_0 \cos i(R), \tag{A11}$$

$$l_{z'}(R) = -\sin i_0 \sin i(R) \cos(\mathrm{PA}(R) - \mathrm{PA}_0) + \cos i_0 \cos i(R). \tag{A12}$$

The tilt and twist angles are then

$$\beta(R) = \arccos(l_{z'}(R)), \tag{A13}$$

$$\gamma(R) = \arctan 2(l_{y'}(R),\ l_{x'}(R)). \tag{A14}$$

In the limit of small perturbations $\delta i(R), \delta\mathrm{PA}(R) \ll 1$, we may expand these expressions to obtain

$$l_{x'}(R) \approx -\sin i_0\, \delta\mathrm{PA}(R), \tag{A15}$$

$$l_{y'}(R) \approx \delta i(R), \tag{A16}$$

$$l_{z'}(R) \approx 1 - \frac{1}{2}[\delta i(R)^2 + \delta\mathrm{PA}(R)^2 \sin^2 i_0]. \tag{A17}$$

Hence,

$$\beta(R) \approx \sqrt{\delta i(R)^2 + \delta\mathrm{PA}(R)^2 \sin^2 i_0}, \tag{A18}$$

$$\gamma(R) \approx \arctan 2(\delta i(R), -\sin i_0\, \delta\mathrm{PA}(R)). \tag{A19}$$

These expressions provide a mapping from the sky-projected disk orientation to a physical representation of the warp in terms of tilt and twist.

A.3. Warp Amplitude

Another useful quantity relating to the geometry of the warp is defined (G. I. Ogilvie 1999):

$$\boldsymbol{\psi}(R) \equiv R \frac{d\boldsymbol{l}}{dR}, \tag{A20}$$

or in our case,

$$\boldsymbol{\psi}(R) = R \begin{pmatrix} -\cos i \sin \mathrm{PA}\, \frac{\partial i}{\partial R} - \sin i \cos \mathrm{PA}\, \frac{\partial \mathrm{PA}}{\partial R} \\ \cos i \cos \mathrm{PA}\, \frac{\partial i}{\partial R} - \sin i \sin \mathrm{PA}\, \frac{\partial \mathrm{PA}}{\partial R} \\ -\sin i\, \frac{\partial i}{\partial R} \end{pmatrix}. \tag{A21}$$

The magnitude of this vector is then

$$\psi(R) = R \sqrt{\left(\frac{\partial i}{\partial R}\right)^2 + \sin^2 i(R) \left(\frac{\partial \mathrm{PA}}{\partial R}\right)^2}. \tag{A22}$$

Although it is a measure of the rate at which the warp changes angle with $\ln R$, for the sake of this work we will describe this as the warp amplitude for consistency with the literature. Some works have related this quantity to stability criteria for a warped disk, which depends on the effective viscosity that may be a product of the warp itself. We do not attempt a stability analysis here, but Equations (A18), (A19), and (A22) constitute a mapping from our observational coordinates into a physical warp structure.

Appendix B
Constructing Radiative Transfer Models

In Section 3.1.2 we discuss our application of radiative transfer calculations to model the scattered light spirals in MWC 758. As noted in that section, our warp model must be extended (extrapolated) into the inner disk in order to capture the region where the warp casts shadows on the scattered light region. Since we are performing not a parameter space study but a proof concept, we choose a very simple approach. We simply fix two values of δi and δPA at two locations interior to our kinematic warp constraint. We then perform a cubic interpolation between the radii to produce a smooth profile, as shown in Figure B1. The choices of fixed points are arbitrarily chosen to produce a sensible profile, while visually attempting to estimate a warp that would produce shadows.

We show a density slice of our density profile used for our radiative transfer model in Figure B2. The blue line traces the midplane, as defined by the highest density at a fixed radius. The amplitude and structure of the warp remain comparable in the inner disk and outer disk. Physically, this need not be the case; there may be tearing or a more complex structure in the inner disk.

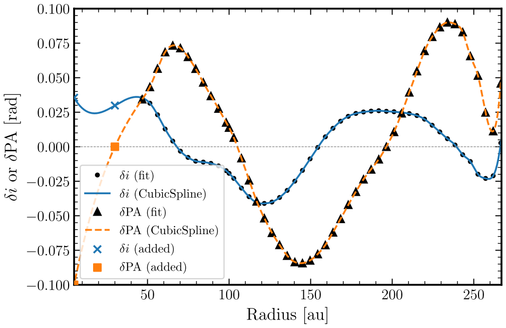

Figure B1. The extrapolation of the warp file we infer for MWC 758 into the inner disk, as required by our radiative transfer model. The two inner points were chosen arbitrarily to extrapolate the warp profile with a cubic spline.

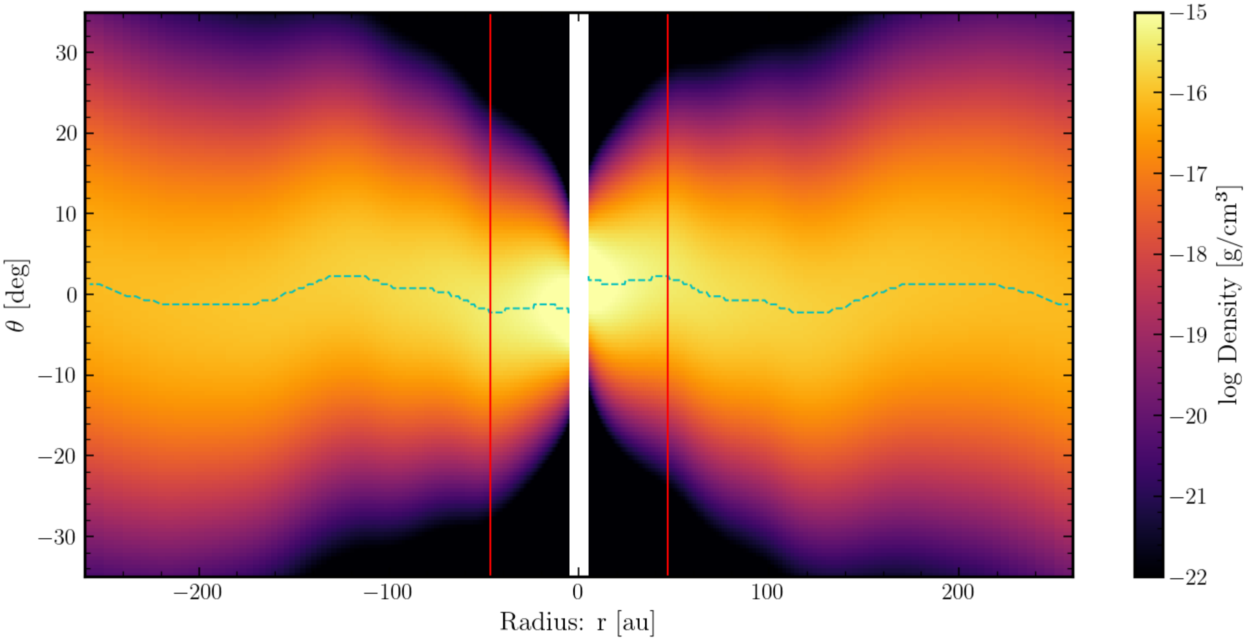

Figure B2. Slice of our model density profile used for radiative transfer calculations of scattered light. The red line shows the radius beyond which we directly use the inferred inclination and position angle profile from the residual LOS velocity map. Inside of this we make an arbitrary cubic spline extrapolation. The cyan dashed line traces the midplane. We use a flaring exponent of 1.03 and a midplane density profile $\propto r^{-1}$.

Appendix C
Catalog of Model Fits

All of the exoALMA sample sources are displayed in the figure set associated with Figure 1. The figure set shows the ^{12}CO and then the ^{13}CO for each disk sequentially, all for a 0.″15 beam that is the fiducial value used in this work. The spatial ranges are determined by where the data become noisy and therefore do not necessarily match between different isotopes. Color scales for the LOS velocity are kept fixed.

C.1. AA Tau

AA Tau is an example where there is already clear evidence for disk warping, with continuum rings (R. A. Loomis et al. 2017) misaligned with respect to both the scattered light (A. W. Cox et al. 2013) and the inner disk (M. O'Sullivan et al. 2005) by around 10°. As suggested by P. Curone et al. (2025), this misalignment appears to cast shadows on the continuum rings. The misalignment has also been suggested as the explanation for substantial photometric variability (J. Bouvier et al. 1999).

AA Tau is a complex disk to analyze kinematically owing to the visible back side in ^{12}CO line emission, being at a high inclination $i_0 \approx -59°$. The Keplerian LOS model results in complex residuals that are a hazard of fitting disk properties in this case. The warp model reproduces aspects of the rotation curve, such as strong nonaxisymmetric features in the inner 50 au, particularly in the top half, where the back side has not been as problematic. The outer disk exhibits symmetry ($m = 2$ periodicity on the annulus), indicating that either a more complex warp model or an alternative must explain these features. While the inclination profile does show some systematic trend in inclination, it is overlaid with large-amplitude, small-scale modulations that may be indicative of other localized structures. The nominal tilt amplitude is 6.°2 ± 0.°4 assuming that the structure is predominantly produced by a warp. This is slightly lower than the ∼10° difference between the inner and outer disks based on scattered light observations, but we are not sensitive down to the very inner disk regions.

C.2. CQ Tau

A. J. Bohn et al. (2022) showed with VLTI/GRAVITY and ALMA observations that CQ Tau has a substantially misaligned disk, making it another convincing case of disk warping. It is morphologically similar to MWC 758, and the warp model does a good job of reproducing the $m = 1$ spiral-like structure. The inclination profile is similarly sinusoidal, with total tilt amplitude 3.°0 ± 0.°3.

C.3. DM Tau

DM Tau is notable for being one of the few disks with directly detectable levels of turbulence via the molecular line widths of the outer disk regions, implying a high turbulent α (K. Flaherty et al. 2020). Similarly to AA Tau, DM Tau suffers from back-side contamination and has been extracted with a double bell line profile (A. F. Izquierdo et al. 2025). At intermediate radii, a similar $m = 2$ symmetry also defies the simple warp model. Unlike AA Tau, however, the warp is a more plausible explanation for the structure in the very outer disk, where the back-side contaminated structure resembles $m = 1$ periodicity. Outside of the inner 100 au, the inclination profile also appears more suggestive of a large-scale warp, showing a systematic linear trend with tilt amplitude 3.°6 ± 0.°2.

C.4. HD 34282

While HD 34282 also suffers from back-side contamination, it also shows a lot of $m = 1$ symmetry that may be indicative of a warp. The warp model does a good job of reproducing the major features. The inclination profile is also coherent across the entire disk scale, again suggestive that a warp could be an appropriate model. However, assuming that this interpretation is correct, HD 34282 exhibits a large tilt amplitude of 7.°4 ± 0.°3, which is much larger than typical of disks for which back-side emission is not visible.

C.5. HD 135344B

HD 135344B is the secondary component of a visual binary, with separation ∼3000 au. It is known to have an inner disk that is misaligned compared to the outer disk (D. Fedele et al. 2008; C. A. Grady et al. 2009; A. Müller et al. 2011). It also has impressive spirals and shadows in the scattered light, as revealed by VLT/SPHERE (T. Stolker et al. 2016). This makes it another highly plausible kinematic warp candidate.

As shown in Figure ??, the warp model does a good job of reproducing the global structure around HD 135344B, although clearly it cannot reproduce the localized vortex (L. Wolfer et al. 2025) or Doppler flip (this feature will be discussed further by A. F. Izquierdo et al. 2025, in preparation). The inclination profile is again linear, suggestive of a large-scale warp, but with moderate amplitude 1.°6 ± 0.°1.

C.6. HD 143006

HD 143006 is another disk that is known to have a misalignment between the inner and outer disks, as evidenced in the shadows observed with VLT/SPHERE (M. Benisty et al. 2018) and VLTI/PIONIER (I. Codron et al. 2025), as well as inferred from the continuum ring geometry (L. M. Pérez et al. 2018). G. Ballabio et al. (2021) had success modeling this system as an inner misaligned binary ($\lesssim$10 au) plus an outer planet. We highlight that in this work we are here sensitive to minor warping in the outer disk and not potentially strong misalignments in the inner regions. The global kinematic structure around HD 143006 is again well produced by a warp, this time with an amplitude of only 1.°1 ± 0.°1.

C.7. J1604

J1604 has a misaligned inner disk with respect to the outer disk (S. Mayama et al. 2018), as well as shadows with temporal variability (P. Pinilla et al. 2018; H. Zhong et al. 2024). These moving shadows were successfully modeled by R. Nealon et al. (2020) as a warp in a circumbinary disk. J. Stadler et al. (2023) also presented kinematic evidence for a planet toward the inner edge of the dust cavity.

Here we find that the global warp again does a good job of reproducing J1604, although whether it can reproduce the structures around 150 au depends on whether this is interpreted as a ring or tightly wound spiral (J. Stadler et al. 2023). Again, only a small inclination of 0.°61 ± 0.°04 is required. The residuals from the warp model seem to suggest a strong wind signature in the outer disk (large negative v_z). If there are also substantial radial velocities arising from the wind, this may enhance the nominal warp tilt we infer outside ∼170 au.

C.8. J1615

In scattered light observations J1615 exhibits distinctive rings that have been suggested to be an indication of truncation by an outer companion (J. de Boer et al. 2016). Despite the back-side contamination, J1615 is reproduced well by the warp model. The inclination profile is very linear in radius, consistent with a large-scale warp with $3\overset{\circ}{.}6 \pm 0\overset{\circ}{.}1$ amplitude.

C.9. J1842

J1842 is again fairly well reproduced by a warp model despite back-side contamination, with a total tilt amplitude of $3\overset{\circ}{.}6 \pm 0\overset{\circ}{.}3$.

C.10. J1852

The LOS velocity structure for J1852 is consistent with a moderate tilt amplitude of $1\overset{\circ}{.}7 \pm 0\overset{\circ}{.}2$. However, it appears very flat except in the very inner regions ($\lesssim$70 au). Even with this inner warp, J1852 is one of the least warped disks in the exoALMA sample.

C.11. LkCa 15

LkCa 15 is another system known to have a warp in the very inner disk regions (S. H. P. Alencar et al. 2018), while its status as a protoplanet host remains debated (e.g., T. Currie et al. 2019; C. H. Gardner et al. 2025). It has a nominal tilt amplitude of $5\overset{\circ}{.}6 \pm 0\overset{\circ}{.}1$, but this may be overestimated because of the strong back-side contribution to the residual velocity map.

C.12. PDS 66

PDS 66 is notable for its apparent lack of substructure in the continuum (Á. Ribas et al. 2023; P. Curone et al. 2025), although it does show a ring-like structure in the scattered light (H. Avenhaus et al. 2018). This structure is quite symmetric, however, and Á. Ribas et al. (2023) suggest that it may be the result of a shadow cast by a puffed-up inner disk. PDS 66 is also one of the quieter exoALMA disks. It exhibits a nominal tilt amplitude of $1\overset{\circ}{.}4 \pm 0\overset{\circ}{.}1$.

C.13. SY Cha

R. Orihara et al. (2023) already suggested that the inner regions of the SY Cha system may be warped, based on their high-resolution ALMA Band 6 kinematic study. K. R. Schwarz et al. (2024) also presented a comparison of JWST/MIRI and archival Spitzer data that showed evidence of strong inner disk variability. Our fitting procedure suggests that SY Cha has the largest tilt amplitude ($10\overset{\circ}{.}2 \pm 0\overset{\circ}{.}5$) of the sample, despite substantial noise from the back-side contribution.

However, we also see that when the warp model is extracted we recover a systematically red inner disk region and a blue outer region. As in the cases of MWC 758 and J1604, this may be the result of a small error in the systemic velocity and an outer wind with a strong negative LOS velocity residual. The difference for SY Cha is that if this interpretation is correct, the outer wind may be present for a substantial fraction of the disk. Interestingly, recent JWST observations revealed extended H_2 and [Ne II] emission around SY Cha, suggestive of a large-scale wind (K. R. Schwarz et al. 2025). In this case, the residual we attribute to a warp may be strongly sub-Keplerian rotation due to the outflowing gas. The warp tilt is greatest in the hypothetical "wind" region outside of 300 au, so the tilt amplitude for SY Cha may be substantially overestimated owing to sub-Keplerian rotation.

C.14. V4046 Sgr

V4046 Sgr is a binary system with a period of 2.4 days (H. C. Stempels & G. F. Gahm 2004), too short to influence the outer disk. The latter is very quiet kinematically, and the tilt amplitude is $0\overset{\circ}{.}87 \pm 0\overset{\circ}{.}02$.

ORCID iDs

Andrew J. Winter https://orcid.org/0000-0002-7501-9801
Myriam Benisty https://orcid.org/0000-0002-7695-7605
Andrés F. Izquierdo https://orcid.org/0000-0001-8446-3026
Giuseppe Lodato https://orcid.org/0000-0002-2357-7692
Richard Teague https://orcid.org/0000-0003-1534-5186
Carolin N. Kimmig https://orcid.org/0000-0001-9071-1508
Sean M. Andrews https://orcid.org/0009-0000-7872-3493
Jaehan Bae https://orcid.org/0000-0001-7258-770X
Marcelo Barraza-Alfaro https://orcid.org/0000-0001-6378-7873
Nicolás Cuello https://orcid.org/0000-0003-3713-8073
Pietro Curone https://orcid.org/0000-0003-2045-2154
Ian Czekala https://orcid.org/0000-0002-1483-8811
Stefano Facchini https://orcid.org/0000-0003-4689-2684
Daniele Fasano https://orcid.org/0000-0003-4679-4072
Cassandra Hall https://orcid.org/0000-0002-8138-0425
Caitlyn Hardiman https://orcid.org/0009-0003-7403-9207
Thomas Hilder https://orcid.org/0000-0001-7641-5235
John D. Ilee https://orcid.org/0000-0003-1008-1142
Misato Fukagawa https://orcid.org/0000-0003-1117-9213
Cristiano Longarini https://orcid.org/0000-0003-4663-0318
François Ménard https://orcid.org/0000-0002-1637-7393
Ryuta Orihara https://orcid.org/0000-0003-4039-8933
Christophe Pinte https://orcid.org/0000-0001-5907-5179
Daniel J. Price https://orcid.org/0000-0002-4716-4235
Giovanni Rosotti https://orcid.org/0000-0003-4853-5736
Jochen Stadler https://orcid.org/0000-0002-0491-143X
David J. Wilner https://orcid.org/0000-0003-1526-7587
Lisa Wölfer https://orcid.org/0000-0002-7212-2416
Hsi-Wei Yen https://orcid.org/0000-0003-1412-893X
Tomohiro C. Yoshida https://orcid.org/0000-0001-8002-8473
Brianna Zawadzki https://orcid.org/0000-0001-9319-1296

References

Alencar, S. H. P., Bouvier, J., Donati, J. F., et al. 2018, A&A, 620, A195
Almendros-Abad, V., Manara, C. F., Testi, L., et al. 2024, A&A, 685, A118
Aly, H., Nealon, R., & Gonzalez, J.-F. 2024, MNRAS, 527, 4777
Ansdell, M., Gaidos, E., Rappaport, S. A., et al. 2016a, ApJ, 816, 69
Ansdell, M., Gaidos, E., Williams, J. P., et al. 2016b, MNRAS, 462, L101
Armitage, P. J., & Pringle, J. E. 1997, ApJL, 488, L47
Avenhaus, H., Quanz, S. P., Garufi, A., et al. 2018, ApJ, 863, 44
Ballabio, G., Nealon, R., Alexander, R. D., et al. 2021, MNRAS, 504, 888
Barraza-Alfaro, M., Flock, M., Béthune, W., et al. 2025, ApJL, 984, L21
Bate, M. R., Lodato, G., & Pringle, J. E. 2010, MNRAS, 401, 1505
Begeman, K. G. 1989, A&A, 223, 47
Benisty, M., Dominik, C., Follette, K., et al. 2023, in ASP Conf. Ser. 534, Protostars and Planets VII, ed. S. Inutsuka et al. (San Francisco, CA: ASP), 605
Benisty, M., Juhasz, A., Boccaletti, A., et al. 2015, A&A, 578, L6
Benisty, M., Juhász, A., Facchini, S., et al. 2018, A&A, 619, A171

Bohn, A. J., Benisty, M., Perraut, K., et al. 2022, A&A, 658, A183
Bouvier, J., Chelli, A., Allain, S., et al. 1999, A&A, 349, 619
Bouvier, J., Grankin, K., Ellerbroek, L. E., Bouy, H., & Barrado, D. 2013, A&A, 557, A77
Casassus, S. 2022, ConeRot: Velocity perturbations extractor, Astrophysics Source Code Library, ascl:2207.027
Casassus, S., Avenhaus, H., Pérez, S., et al. 2018, MNRAS, 477, 5104
Casassus, S., Marino, S., Pérez, S., et al. 2015, ApJ, 811, 92
Casassus, S., & Pérez, S. 2019, ApJL, 883, L41
Codron, I., Kraus, S., Monnier, J. D., et al. 2025, MNRAS, 541, 1600
Cody, A. M., Stauffer, J., Baglin, A., et al. 2014, AJ, 147, 82
Cox, A. W., Grady, C. A., Hammel, H. B., et al. 2013, ApJ, 762, 40
Cuello, N., Ménard, F., & Price, D. J. 2023, EPJP, 138, 11
Curone, P., Facchini, S., Andrews, S. M., et al. 2025, ApJL, 984, L9
Currie, T., Marois, C., Cieza, L., et al. 2019, ApJL, 877, L3
de Boer, J., Salter, G., Benisty, M., et al. 2016, A&A, 595, A114
Debes, J., Nealon, R., Alexander, R., et al. 2023, ApJ, 948, 36
Debes, J. H., Jang-Condell, H., & Schneider, G. 2016, ApJL, 819, L1
Delfini, L., Vioque, M., Ribas, Á., & Hodgkin, S. 2025, A&A, 699, A145
Deng, H., & Ogilvie, G. I. 2022, MNRAS, 512, 6078
Donati, J. F., Gregory, S. G., Montmerle, T., et al. 2011, MNRAS, 417, 1747
Donehew, B., & Brittain, S. 2011, AJ, 141, 46
Dorschner, J., Begemann, B., Henning, T., Jaeger, C., & Mutschke, H. 1995, A&A, 300, 503
Doğan, S., Nixon, C. J., King, A. R., & Pringle, J. E. 2018, MNRAS, 476, 1519
Doğan, S., Nixon, C. J., King, A. R., Pringle, J. E., & Price, D. 2023, in IAU Symp. 362, The Predictive Power of Computational Astrophysics as a Discover Tool, ed. D. Bisikalo, D. Wiebe, & C. Boily (Cambridge: Cambridge Univ. Press), 177
Dullemond, C. P., Juhasz, A., Pohl, A., et al. 2012, RADMC-3D: A multi-purpose radiative transfer tool, Astrophysics Source Code Library, ascl:1202.015
Dullemond, C. P., Kimmig, C. N., & Zanazzi, J. J. 2022, MNRAS, 511, 2925
Facchini, S., Juhász, A., & Lodato, G. 2018, MNRAS, 473, 4459
Facchini, S., Lodato, G., & Price, D. J. 2013, MNRAS, 433, 2142
Fairlamb, J. R., Oudmaijer, R. D., Mendigutìa, I., Ilee, J. D., & van den Ancker, M. E. 2015, MNRAS, 453, 976
Fedele, D., van den Ancker, M. E., Acke, B., et al. 2008, A&A, 491, 809
Flaherty, K., Hughes, A. M., Simon, J. B., et al. 2020, ApJ, 895, 109
Foucart, F., & Lai, D. 2011, MNRAS, 412, 2799
Galloway-Sprietsma, M., Bae, J., Izquierdo, A. F., et al. 2025, ApJL, 984, L10
Gardner, C. H., Isella, A., Li, H., et al. 2025, ApJL, 984, L16
Garufi, A., Benisty, M., Pinilla, P., et al. 2018, A&A, 620, A94
Garufi, A., Ginski, C., van Holstein, R. G., et al. 2024, A&A, 685, A53
Ginski, C., Facchini, S., Huang, J., et al. 2021, ApJL, 908, L25
Grady, C. A., Schneider, G., Sitko, M. L., et al. 2009, ApJ, 699, 1822
Harris, C. R., Millman, K. J., van der Walt, S. J., et al. 2020, Natur, 585, 357
Haworth, T. J., Facchini, S., Clarke, C. J., & Cleeves, L. I. 2017, MNRAS, 468, L108
Held, L. E., & Ogilvie, G. I. 2024, MNRAS, 535, 3108
Huélamo, N., Chauvin, G., Schmid, H. M., et al. 2018, A&A, 613, L5
Ingleby, L., Calvet, N., Herczeg, G., et al. 2013, ApJ, 767, 112
Izquierdo, A. F., Stadler, J., Galloway-Sprietsma, M., et al. 2025, ApJL, 984, L8
Izquierdo, A. F., Testi, L., Facchini, S., Rosotti, G. P., & van Dishoeck, E. F. 2021, A&A, 650, A179
Jaeger, C., Mutschke, H., Begemann, B., Dorschner, J., & Henning, T. 1994, A&A, 292, 641
Juhász, A., & Facchini, S. 2017, MNRAS, 466, 4053
Kimmig, C. N., & Dullemond, C. P. 2024, A&A, 689, A45
Kimmig, C. N., & Villenave, M. 2025, A&A, 698, A146
Kraus, S., Kreplin, A., Young, A. K., et al. 2020, Sci, 369, 1233
Kuffmeier, M., Jensen, S. S., & Haugbølle, T. 2023, EPJP, 138, 272
Kuffmeier, M., Pineda, J. E., Segura-Cox, D., & Haugbølle, T. 2024, A&A, 690, A297
Lai, D. 1999, ApJ, 524, 1030
Lazareff, B., Berger, J. P., Kluska, J., et al. 2017, A&A, 599, A85
Lodato, G., & Facchini, S. 2013, MNRAS, 433, 2157
Lodato, G., & Price, D. J. 2010, MNRAS, 405, 1212
Lodato, G., & Pringle, J. E. 2006, MNRAS, 368, 1196
Lodato, G., & Pringle, J. E. 2007, MNRAS, 381, 1287
Lodato, G., Rampinelli, L., Viscardi, E., et al. 2023, MNRAS, 518, 4481
Longarini, C., Lodato, G., Rosotti, G., et al. 2025, ApJL, 984, L17
Longarini, C., Lodato, G., Toci, C., & Aly, H. 2021, MNRAS, 503, 4930
Loomis, R. A., Facchini, S., Benisty, M., et al. 2025, ApJL, 984, L7
Loomis, R. A., Öberg, K. I., Andrews, S. M., & MacGregor, M. A. 2017, ApJ, 840, 23
Lubow, S. H., & Ogilvie, G. I. 2000, ApJ, 538, 326
Manara, C. F., Ansdell, M., Rosotti, G. P., et al. 2023, in ASP Conf. Ser. 534, Protostars and Planets VII, ed. S. Inutsuka et al. (San Francisco, CA: ASP), 539
Manara, C. F., Testi, L., Herczeg, G. J., et al. 2017, A&A, 604, A127
Manara, C. F., Testi, L., Natta, A., et al. 2014, A&A, 568, A18
Martire, P., Longarini, C., Lodato, G., et al. 2024, A&A, 686, A9
Mayama, S., Akiyama, E., Panić, O., et al. 2018, ApJL, 868, L3
Müller, A., van den Ancker, M. E., Launhardt, R., et al. 2011, A&A, 530, A85
Muro-Arena, G. A., Benisty, M., Ginski, C., et al. 2020, A&A, 635, A121
Nealon, R., Dipierro, G., Alexander, R., Martin, R. G., & Nixon, C. 2018, MNRAS, 481, 20
Nealon, R., Pinte, C., Alexander, R., Mentiplay, D., & Dipierro, G. 2019, MNRAS, 484, 4951
Nealon, R., Price, D. J., & Pinte, C. 2020, MNRAS, 493, L143
Nixon, C., King, A., & Price, D. 2013, MNRAS, 434, 1946
Ogilvie, G. I. 1999, MNRAS, 304, 557
Ogilvie, G. I., & Latter, H. N. 2013, MNRAS, 433, 2403
Orihara, R., & Momose, M. 2025, ApJ, 986, 215
Orihara, R., Momose, M., Muto, T., et al. 2023, PASJ, 75, 424
O'Sullivan, M., Truss, M., Walker, C., et al. 2005, MNRAS, 358, 632
Paardekooper, S.-J., & Ogilvie, G. I. 2019, MNRAS, 483, 3738
Papaloizou, J. C. B., & Pringle, J. E. 1983, MNRAS, 202, 1181
Pedregosa, F., Varoquaux, G., Gramfort, A., et al. 2011, JMLR, 12, 2825
Pérez, L. M., Benisty, M., Andrews, S. M., et al. 2018, ApJL, 869, L50
Pineda, J. E., Quanz, S. P., Meru, F., et al. 2014, ApJL, 788, L34
Pinilla, P., Benisty, M., de Boer, J., et al. 2018, ApJ, 868, 85
Pinte, C., Ilee, J. D., Huang, J., et al. 2025, ApJL, 984, L15
Pinte, C., Price, D. J., Ménard, F., et al. 2018, ApJL, 860, L13
Pinte, C., Price, D. J., Ménard, F., et al. 2020, ApJL, 890, L9
Price, D. J., Cuello, N., Pinte, C., et al. 2018, MNRAS, 477, 1270
Pringle, J. E. 1996, MNRAS, 281, 357
Ren, B. B., Benisty, M., Ginski, C., et al. 2023, A&A, 680, A114
Ren, B. B., Xie, C., Benisty, M., et al. 2024, A&A, 681, L2
Ribas, Á., Macìas, E., Weber, P., et al. 2023, A&A, 673, A77
Rigliaco, E., Pascucci, I., Duchene, G., et al. 2015, ApJ, 801, 31
Rogers, C., de Marchi, G., & Brandl, B. 2025, A&A, 698, A172
Romanova, M. M., Koldoba, A. V., Ustyugova, G. V., et al. 2021, MNRAS, 506, 372
Rosenfeld, K. A., Chiang, E., & Andrews, S. M. 2014, ApJ, 782, 62
Rosotti, G. P., Dale, J. E., de Juan Ovelar, M., et al. 2014, MNRAS, 441, 2094
Sakai, N., Oya, Y., Sakai, T., et al. 2014, ApJL, 791, L38
Schwarz, K. R., Henning, T., Christiaens, V., et al. 2024, ApJ, 962, 8
Schwarz, K. R., Samland, M., Olofsson, G., et al. 2025, ApJ, 980, 148
Shuai, L., Ren, B. B., Dong, R., et al. 2022, ApJS, 263, 31
Sicilia-Aguilar, A., Manara, C. F., de Boer, J., et al. 2020, A&A, 633, A37
Sitko, M. L., Day, A. N., Kimes, R. L., et al. 2012, ApJ, 745, 29
Stadler, J., Benisty, M., Izquierdo, A., et al. 2023, A&A, 670, L1
Stadler, J., Benisty, M., Winter, A. J., et al. 2025, ApJL, 984, L11
Stauffer, J., Cody, A. M., McGinnis, P., et al. 2015, AJ, 149, 130
Stempels, H. C., & Gahm, G. F. 2004, A&A, 421, 1159
Stolker, T., Dominik, C., Avenhaus, H., et al. 2016, A&A, 595, A113
Teague, R., Bae, J., Andrews, S. M., et al. 2022, ApJ, 936, 163
Teague, R., Benisty, M., Facchini, S., et al. 2025, ApJL, 984, L6
Veronesi, B., Longarini, C., Lodato, G., et al. 2024, A&A, 688, 136
Villenave, M., Podio, L., Duchêne, G., et al. 2023, ApJ, 946, 70
Watson, A. M., & Stapelfeldt, K. R. 2007, AJ, 133, 845
Winter, A. J., Benisty, M., Manara, C. F., & Gupta, A. 2024a, A&A, 691, A169
Winter, A. J., Benisty, M., Shuai, L., et al. 2024b, A&A, 691, A43
Wolfer, L., Barraza-Alfaro, M., Teague, R., et al. 2025, ApJL, 984, L22
Young, A. K., Alexander, R., Rosotti, G., & Pinte, C. 2022, MNRAS, 513, 487
Young, A. K., Alexander, R., Walsh, C., et al. 2021, MNRAS, 505, 4821
Young, A. K., Stevenson, S., Nixon, C. J., & Rice, K. 2023, MNRAS, 525, 2616
Zagaria, F., Jiang, H., Cataldi, G., et al. 2025, arXiv:2506.16481
Zawadzki, B., Czekala, I., Galloway-Sprietsma, M., et al. 2025, ApJL, 984, L14
Zhang, S., & Zhu, Z. 2024, ApJL, 974, L38
Zhong, H., Ren, B. B., Ma, B., et al. 2024, A&A, 684, A168
Zhu, Z. 2019, MNRAS, 483, 4221
Ziampras, A., Dullemond, C. P., Birnstiel, T., Benisty, M., & Nelson, R. P. 2025, MNRAS, 540, 1185
Zuleta, A., Birnstiel, T., & Teague, R. 2024, A&A, 692, A56